國立臺灣大學電機資訊學院光電工程學研究所

碩士論文

Graduate Institute of Photonics and Optoelectronics
College of Electrical Engineering and Computer Science
National Taiwan University

Master Thesis

以緊束縛近似法計算矽和二硫化鉬的能帶結構與電性質

Tight Binding Calculations of Silicon and MoS_2 Band Structure and Electronic Properties

陳爍帆

Shuo-Fan Chen

指導教授：吳育任 博士

Advisor: Yuh-Renn Wu, Ph.D.

中華民國 105 年 7 月

July, 2016

doi:10.6342/NTU201700233

doi:10.6342/NTU201700233

誌謝

碩士論文，記錄了兩年來的努力，也是獻給臺大最後的餞別禮，六年，是時候與臺大道別了。 一切從兩年前開始，帶著抱負與期待加入實驗室，接手了全新的題目。從一無所知開始，閱讀期刊、教科書、與老師討論，到慢慢進入狀況，進度稍有眉目，過程中也曾遭遇難解的問題、甚至方向錯誤，但很幸運最後能成功建構模型並得到結果，在產學合作計畫、研討會、甚至國際期刊發表。 兩年來，首先要感謝吳育任教授，從研究論文題目中我閱讀了大量文獻，也在思考方法、與老師討論的過程中領悟許多細節。接著要感謝實驗室的同仁們，德仁身爲老師愛將總是熱心爲大家處理實驗室瑣事，理碩常在意外的時間出現激勵大家、邀請大家開工上班，實驗室主力冠穎則幫大家扛住要命的計畫，彥璋雖然遠在中研院，也總在必要的時刻出現緩和氣氛，另外有實驗室傳奇學長鎮國給了我許多實用建議，樂觀樸實的仲成則留下許多津津樂道的故事，學弟志維則扮演著實驗室氣氛的舵手，另外特別感謝大學長季剛，熱心教導後生各種知識技能，也樂於分享在學術界打滾的經驗。最後當然要感謝父母，對我的任何決定都給予支持，也體諒我回家時間很短促，讓我的研究生生涯無所顧慮。 最後感謝臺大帶給我們的視野與抱負，一日臺大人，終身臺大人。

doi:10.6342/NTU201700233

摘要

多年以來，半導體元件的推導大都基於泊松方程和電流平衡方程式的迭代，通常將材料視爲完美晶格，如此一來能帶圖和相對應的能帶密度、載子有效質量和載子濃度都可以被寫成解析解。然而當金氧半場效電晶體的尺度到達原子等級，基於多體物理且運算量適當的模型將迫切需求，此模型必須將原子的週期位能效應考慮進薛丁格方程式的哈密頓算符中，並選取適當基底求解方程，在所有方法中，緊束縛近似法是最普遍的。在這篇論文中，我們將應用緊束縛近似法來計算矽奈米線的能帶和有效質量，以此研究不同寬度下，量子侷限效應對矽奈米線的影響，結果顯示量子侷限效應將增大材料的能隙和載子有效質量，且因於矽在不同方向的電子傳輸有效質量不同，量子侷限效應將改變傳導帶最低能態在倒置晶格空間中的位子。我們進一步將此模型應用於二硫化鉬上，二硫化鉬是一種具有很好的機械性質的二維材料，它可以承受很大的應力 (最高到12%)，且它的奈米帶結構具有特別的表面特性，因此我們將緊束縛近似法應用在二硫化鉬和它的奈米帶結構上，來研究它的應力效應和表面性質，結果顯示外加拉伸應力會減小能隙和載子有效質量，然而主導價帶在倒置晶格空間中位子的改變，反而大幅增加電洞的有效質量。

doi:10.6342/NTU201700233

ABSTRACT

For several decades, the semiconductor device theory was basically based on semi-classical model, where Poisson, drift-diffusion, and Schrödinger equation with effective mass or k.p method are solved to obtain the solution. The materials were often treated as perfect crystals, then the E-k relation and factors like density of state, effective mass and carrier density can all be written as analytical terms. However, as the dimensions of metal-oxide field effect transistors reach a few atomic scale, a model considering many-body physics with a reasonable time consumption is necessary. The new method needs to include the atomic potential into the Schrödinger Hamiltonian, then choose a suitable basis to solve the eigenvalue problem. Among all these approaches, the Tight Binding method (TBM) is the most popular. TBM directly uses the atomic orbital as the basis, and assumes that the potential is bonded tightly at the central atom.

In this paper, we applied the tight binding method to silicon nanowires, and calculated the bandgap, effective mass and density of states. We studied the quantum confinement effect on the nanowires with different width, and compared to the infinite quantum well and the perfect

doi:10.6342/NTU201700233

crystal models. The results show that the quantum confinement effect will enlarge the bandgap and the carrier effective mass, and also rearrange the conduction band edge position in the k-space due to the effective mass difference between the lateral and perpendicular directions.

Then we further applied our model to the novel 2D material. Molybdenum disulfide (MoS_2) is a 2D material with good mechanical and chemical properties. It can endure a large strain (12%), and its nanoribbon structure has interesting edge properties. So we applied TBM to MoS_2 and its nanoribbon to study the strain effects and edge states properties. The results show that the tensile strain can make the bandgap and the carrier effective mass smaller; however, the K-to-Γ valley transition at the valence band edge gives it a larger hole effective mass.

doi:10.6342/NTU201700233

目　　　　錄

口試委員會審定書 i

誌謝 ii

中文摘要 iii

英文摘要 iv

目錄 vi

圖目錄 viii

表目錄 xiv

1 Introduction 1

1.1 Electronic Band Structure and Basic Semiconductor Physics 1

1.2 Band Theory - First Principle 4

1.3 Tight Binding Method and Bloch States 6

1.4 Tight Binding in Quantum Structures 9

1.5 Molybdenum Disulfide and its Nanoribbon 11

2 Methodology 14

2.1 Tight Binding Hamiltonian: Bulk 14

2.2 Tight Binding Hamiltonian: Nanowire 16

2.3 Strains and Boundary Condition 19

doi:10.6342/NTU201700233

2.4 Effective Mass and Density of States 21

3 Silicon 22

3.1 Bulk Silicon 22

3.2 Silicon Slab and Surface States 23

3.3 Silicon Nanowire 25

3.4 Band Structure under External Potential 30

4 MoS_2 34

4.1 MoS_2 Tight Binding Model 34

4.2 Strain Effects 37

4.3 MoS_2 Nanoribbon 45

4.4 Multi-Layer MoS_2 52

5 Conclusion 55

A.1 Appendices 57

A.1.1 Tight Binding Parameters 57

Bibliography 59

doi:10.6342/NTU201700233

圖 目 錄

1.1 The left figure shows the calculated carrier density by classical Poisson drift-diffusion solver and semi-classical Poisson-Schrödinger solver respectively. The right figure points out the atomic scale potential we ignore when doing semi-classical calculation. 4

1.2 The figure shows the periodicity of a silicon nanowire. The y, z directions are confined with the confined width = W. The x direction is the transport direction with the periodic boundary condition. 11

1.3 The crystal structure of a single-layer MoS_2. The figure was a copyright from [1]. 13

2.1 The interaction energy under different conditions. $\mathbf{R}$ isthe vector between two neighbor atoms, and θ_x is the angle between the bonding vector and the x axis. . . . 16

2.2 The change of periodicity makes the size and the shape of the unit cell different. 18

doi:10.6342/NTU201700233

3.1 Bulk silicon band structures with sp^3s^* [2], sp^3d^5 [3] and $sp^3d^5s^*$ [4] orbital basis respectively. 23

3.2 Quantum slab structure. The plane is large enough to be treated as infinite. 24

3.3 5.5 nm thick quantum slab without surface passivation and with hydrogen passivation. 24

3.4 Silicon nanowire [100] band structure with (a) W = 1.49 nm, (b) W = 2.58 nm and (c) W = 5.30 nm. 25

3.5 Silicon nanowire band gap and conduction band edge effective mass (Γ point) versus the wire width. a is the lattice constant. 26

3.6 [100] direction band structure calculated by the primitive unit cell (2 atoms) and the cube unit cell (8 atoms). 27

3.7 2D projection of the first Brillouin zone (BZ). The blue line is the primitive unit cell BZ, while the brown line is the cube unit cell BZ. 28

3.8 The difference of the transverse effective ($0.19m_0$) and the longitudinal effective mass ($0.98m_0$) for silicon makes the density-of-state effective mass at the six X valleys different. 29

doi:10.6342/NTU201700233

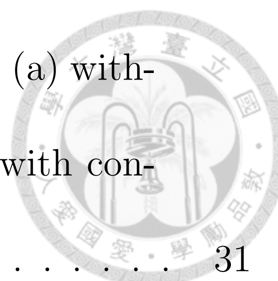

3.9 5.30 nm wide Silicon nanowire band structure (a) without bias, (b) with convex potential, and (c) with concave potential. 31

3.10 An extra potential distributed in the wire cross section will reduce the effective bandgap. It is associated to the Quantum Confinement Stark Effect. 32

3.11 5.30 nm wide Silicon nanowire band structure with different magnitudes of concave potentials. 33

3.12 5.30 nm wide Silicon nanowire conduction band electron wavefunction square (a) without bias, (b) with convex potential, and (c) with concave potential. 33

4.1 Monolayer MoS_2 band structure with different models from reference. 36

4.2 To apply strains in MoS_2, engineers grow MoS_2 on the substrate then give the substrate a compressive strain [5]. 38

4.3 Monolayer MoS_2 under (a) 0%, (b) 1.5%, (c) 6% and (d) 10% biaxial strains on the X-Y lateral plane. 39

doi:10.6342/NTU201700233

4.4 (a) The K-K direct bandgap and the K-Γ indirect bandgap under different biaxial strains. (b) The carrier effective mass at K valley under different biaxial strains. 40

4.5 Monolayer MoS_2 band structures (a) without strains, with (b) 4%, (c) 12% tensile strains at x directions, and (f) 4%, (g) 12% tensile strains at y directions. (d) Structure profile. 41

4.6 2D E-k diagram at the valence band maximum with (a) 0%, (b) 1.5% and (c) 6% uniaxial tensile strains. The direction is shown in the brown double arrow. 42

4.7 (a) The K-K direct bandgap and the K-Γ indirect bandgap under different uniaxial strains. (b) The carrier effective mass at K valley under different uniaxial strains. . 43

4.8 The hole effective mass at Γ valley along Γ to K valley direction with different (a) uniaxial tensile strains (also along Γ to K direction) and (b) biaxial tensile strains. Note that for strain smaller than the red dash line, the effective mass is decided by K valley so we don't list the effective mass of Γ valley 44

doi:10.6342/NTU201700233

4.9 Structures of the zigzag nanoribbon and the armchair nanoribbon. 45

4.10 The MoS_2 armchair nanoribbon density-of-state per area with the widths equal to (a) 1.59 nm, (c) 7.93 nm, (e) 15.9 nm, (g) 31.7 nm, and the band structures with the widths equal to (b) 1.59 nm, (d) 7.93 nm, (f) 15.9 nm, (h)31.7 nm. The inset shows the structure of the armchair nanoribbon. 46

4.11 Wavefunction absolute value versus the atom position. 47

4.12 (a) The carrier effective mass and (b) the bandgap with different nanoribon width. 48

4.13 The MoS_2 armchair nanoribbon density-of-state per area with the uniaxial tensile strains equal to (a) 0%, (c) 4%, (e) 8%, (g) 12%. The band structures with tensile strains equal to (b) 0%, (d) 4%, (f) 8%, (h) 12%. The nanoribbon width is 31.7 nm. The strain is applied along the transport direction. 48

4.14 (a) Sructure profile. (b) Figure explaining the band folding issue. (c) Valence band mzximum under 0%, (d) 4% and (e) 8% tensile strains. 49

doi:10.6342/NTU201700233

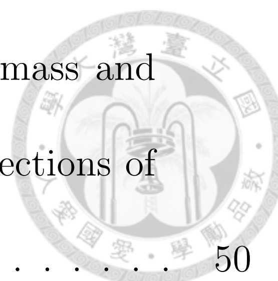

4.15 (a) Structure profile. (b) Electron effective mass and (c) hole effective mass with two different directions of strains. 50
4.16 The density-of-state per area of zigzag nanoribbon with the width equal to (a) 2.75 nm, (c) 6.86 nm, (e) 13.73 nm, and the band structures with nanoribbon width equal to (b) 2.75 nm, (d) 6.86 nm, (f) 13.73 nm. (g) The zigzag structure. 50
4.17 (a) Single-layer and double-layer MoS_2 band structures. (b) Six-layer MoS_2 and bulk MoS_2 band structures. . . . 53
4.18 Density-of-state per area of (a) 1-layer, (c) 5-layer armchair nanoribbon, and the band diagram of (b) 1-layer, (d) 5-layer armchair nanoribbon (width = 3.17 nm). Density-of-state per area of (e) 1-layer, (g) 5-layer zigzag nanoribbon, and the band diagram of (f) 1-layer, (h) 5-layer zigzag nanoribbon (width = 2.75 nm). 54

doi:10.6342/NTU201700233

表　　目　　錄

doi:10.6342/NTU201700233

Chapter 1 Introduction

1.1 Electronic Band Structure and Basic Semiconductor Physics

For decades, the semi-classical model based on Poisson Drift-Diffusion has successfully predicted the behavior of semiconductor devices. To simplify the problem, we need the assumptions like the near-free-electron model and the effective mass approximation. Combined with the concepts of density of states and Fermi-Dirac distribution, then solve the Poisson Drift-Diffusion equation iteratively, the current-voltage relation can be figured out.

According to the near-free-electron model, the electron wavefunction and the corresponding eigen energy are given by

$$\psi\left(\mathbf{r}\right)=\frac{1}{\sqrt{\Omega}}e^{i\mathbf{k}\cdot\mathbf{r}}\ ,\qquad E\left(\mathbf{k}\right)=\frac{\hbar^2k^2}{2m^*}+E_C\ , \tag{1.1.1}$$

where Ω is the normalization factor, and E_C is the reference energy level. In the semiconductor physics it often means the conduction band edge. The later is the so-called E-k relation. With this equation, the density of state can be calculated by the number of electronic states

doi:10.6342/NTU201700233

per unit volume and per unit energy

$$N_{DOS} = \frac{2}{V}\frac{dN}{dE} = \frac{2}{V}\frac{dN}{dk}\frac{dk}{dE}$$
$$= \frac{2}{V}\left(\frac{L}{\pi}\right)^3 \pi k^2 \frac{dk}{dE} = \frac{m^*}{\pi\hbar^2}\frac{\sqrt{2m^*\left(E-E_C\right)}}{\pi\hbar} \tag{1.1.2}$$

Combined with Fermi-Dirac distribution, the carrier density can be calculated by the integral over energy

$$n\left(E\right) = \int_{E_C}^{\infty} N_{DOS}\frac{1}{1+\exp\left(\frac{E-E_F}{k_BT}\right)}$$
$$= 2\left(\frac{2\pi m^* k_B T}{h^2}\right)^{3/2}\exp\left(\frac{E_F-E_C}{k_BT}\right) \ , \tag{1.1.3}$$

where k_B is the Boltzmann constant. To figure out the current-voltage relation, one needs to know the potential distribution (E_C) and the fermi level (E_F) position by solving the Poisson's equation and drift-diffusion equation iteratively.

Poisson's equation:

$$\nabla^2\phi = -\frac{q}{\epsilon}\left(-n+p+N_D^+-N_A^-\right) \tag{1.1.4}$$

Electron current equation:

$$\vec{J}_n = -qn\mu_n\nabla\phi + q\nabla\left(nD_n\right) \ , \ \nabla\cdot\vec{J}_n = 0 \tag{1.1.5}$$

Hole current equation:

$$\vec{J}_p = -qp\mu_p\nabla\phi - q\nabla\left(pD_p\right) \ , \ \nabla\cdot\vec{J}_p = 0 \tag{1.1.6}$$

doi:10.6342/NTU201700233

In the above model, the effective mass (m^*) in the carrier density formula is given by the experimental measurement, and the E-k relation can be written as a simple equation. The model is successful for large dimension devices (> 30 nm). As the devices scale down, the energy distribution in the material will change due to the boundary condition. It will influence the effective mass and the bandgap. One simple way to include the quantum effect is by solving the Schrödinger equation based on the near-free-electron approximation. For example, we can calculate the square nanowire subbands energy by solving the infinite quantum well Schrödinger equation. The subband energy levels are given by

$$E_{n_x,n_y}(k_z) = E_C + \frac{n_x^2\pi^2\hbar^2}{2m^*L_x^2} + \frac{n_y^2\pi^2\hbar^2}{2m^*L_y^2} + \frac{\hbar^2k_z^2}{2m^*} \tag{1.1.7}$$

However, in this method we still use the bulk effective mass. This is not valid in nano scales. Physics considering more details in the crystal potential is necessary.

doi:10.6342/NTU201700233

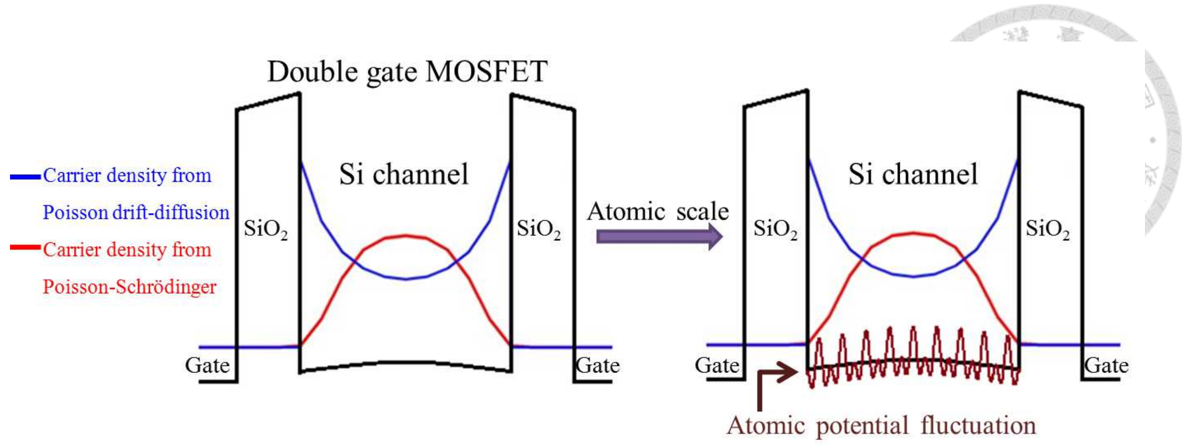

Figure 1.1: The left figure shows the calculated carrier density by classical Poisson drift-diffusion solver and semi-classical Poisson-Schrödinger solver respectively. The right figure points out the atomic scale potential we ignore when doing semi-classical calculation.

1.2 Band Theory - First Principle

In a multielectron and multiatom system, the Hamiltonian has the form

$$H = -\sum_i \frac{\hbar^2}{2m}\nabla_i^2 - \frac{1}{4\pi\epsilon_0}\sum_i \frac{Ze^2}{\|\mathbf{r}_i\|} + \frac{1}{4\pi\epsilon_0}\sum_{i<j}\frac{e^2}{\|\mathbf{r}_i - \mathbf{r}_j\|}\ , \qquad (1.2.1)$$

which contains the interaction between different electrons and different atomic orbitals. Although we hope to take into account the atomic nature of a material, the Hamiltonian in the whole system is so difficult to solve. One popular first principle method to deal with the multi-electron problem is the Kohn—Sham density functional theory (DFT) [6], where the electron-electron interaction effects were taken into account by assuming an effective potential term. The Schrödinger

doi:10.6342/NTU201700233

equation becomes

$$\widehat{H}_{KS}\psi_{i\sigma}(\mathbf{r}) = \left[-\frac{1}{2}\nabla^2 + v_{eff,\sigma}(\mathbf{r})\right]\psi_{i\sigma}(\mathbf{r}) \\ = \varepsilon_{i\sigma}\psi_{i\sigma}(\mathbf{r}), \tag{1.2.2}$$

where $v_{eff,\sigma}(\mathbf{r})$ is the effective KS potential and σ is the spin index. In DFT, the electron density is given as [7]

$$\rho(\mathbf{r}) = \sum_i \mid \phi(\mathbf{r}) \mid^2 , \tag{1.2.3}$$

and the system energy will be

$$E[\rho] = T_s[\rho] + J[\rho] + E_{xc}[\rho] + \int v_{ext}(\mathbf{r})\rho(\mathbf{r})d\mathbf{r}, \tag{1.2.4}$$

where T_s is the kinetic energy term, v_{ext} is the external potential, V_H is the Coulomb energy and E_{xc} is the exchange-correlation energy. The begin with, we guess an initial electron density, then calculate the exchange-correlation energy by a chosen model, finally the ground state energy can be solved iteratively. If the exact form for $E_{xc}[\rho]$ is used, it should be cancelled with $J[\rho]$ in the one-electron system. Even if the exact exchange-correlation energy is a functional of the density, this functional is not known explicitly. Approximations for $E_{xc}[\rho]$ like LDA [8] or GGA [9–11] will generate self-interaction energy [12] and result in an incorrect long-range behavior. So in this thesis we choose the semi-classical tight binding method, which is lack of iterating cal-

doi:10.6342/NTU201700233

culation and can be fitted to the experimental data accurately by using the proper parameters.

1.3 Tight Binding Method and Bloch States

In 1928, F. Bloch combined the wave nature of electrons and the periodic potential to construct the basic form of Schrödinger equation in solids [13]. The theory argued that in a periodic potential $U(\mathbf{r}) = U(\mathbf{r}+\mathbf{R})$, the wavefunction will have the relation $\psi(\mathbf{r}+\mathbf{R}) = e^{i\mathbf{k}\cdot\mathbf{R}}\psi(\mathbf{r})$, where $\mathbf{R}$ is the periodic vector in the lattice. With Bloch theorem, several band structure calculation tools could be developed with different choice of base. For example, the Pseudopotential method [14] assumes an effective potential to replace the complex core potential. The plane-wave method uses plane waves $\psi(\mathbf{r}) = \frac{1}{\sqrt{\Omega}}e^{i(\mathbf{k}-\mathbf{K})\cdot\mathbf{r}}$ as the base.

From the above section, we know that in DFT, one should guess an initial electron density and solve the self-consistent problem. Now suppose that we already know the ground state density ρ^0, and choose the atomic orbitals $\psi_\eta : \eta = s, p_x, p_y, ...$ as a set of basis, assuming the basis is orthogonal, we can easily solve the ground state Schrödinger

doi:10.6342/NTU201700233

equation

$$\left[-\frac{\hbar^2}{2m}\nabla^2 + U^{eff}\left[\rho^0\right]\right]\phi_i = H_0\phi_i = \varepsilon_i\phi_i \ , \tag{1.3.1}$$

where

$$\phi_i = \sum_\eta b_\eta \psi_\eta \tag{1.3.2}$$

Afterwards, we put the remaining unknown terms in the Hamiltonian, the Coulomb interaction and exchange-correlation terms, into the repulsive energy, E^{rep}, we can get the Tight Binding expression

$$E_{TB}\left[\rho\right] = \sum_i \varepsilon_i + E^{rep} = \sum_i \varepsilon_i + \frac{1}{2}\sum_{\alpha\beta} U_{\alpha\beta} \ , \tag{1.3.3}$$

where $U_{\alpha\beta}$ is the interaction energy of different orbital basis.

In bulk semiconductors, one can apply Bloch theorem. With the lattice vector equals to $\mathbf{R}$, the wavefunction then becomes

$$\psi_{\mathbf{k}}\left(\mathbf{r}\right) = \sum_{\mathbf{R}} e^{i\mathbf{k}\cdot\mathbf{R}}\phi\left(\mathbf{r}-\mathbf{R}\right) = \sum_{\mathbf{R},\eta} b_\eta e^{i\mathbf{k}\cdot\mathbf{R}}\psi_\eta\left(\mathbf{r}-\mathbf{R}\right) \tag{1.3.4}$$

and the eigen equation will be

$$H\psi_{\mathbf{k}}\left(\mathbf{r}\right) = E\psi_{\mathbf{k}}\left(\mathbf{r}\right) \ , \ H = H_0 + U\left(\mathbf{r}\right) \tag{1.3.5}$$

After some calculations and ignore the overlap term $\left\langle \psi_\alpha\left(\mathbf{r}\right) \mid \psi_\beta\left(\mathbf{r}-\mathbf{R}\right)\right\rangle_{\mathbf{R}\neq 0}$, we can get the Tight Binding eigen equation

$$\begin{aligned} b_\alpha E\left(\mathbf{k}\right) = b_\alpha\varepsilon_\alpha &+ \sum_\beta b_\beta \int d\mathbf{r}\psi_\alpha^*\left(\mathbf{r}\right)U\left(\mathbf{r}\right)\psi_\beta\left(\mathbf{r}\right) \\ &+ \sum_{\beta,\mathbf{R}\neq 0} b_\beta \int d\mathbf{r}\psi_\alpha^*\left(\mathbf{r}\right)U\left(\mathbf{r}\right)\psi_\beta\left(\mathbf{r}-\mathbf{R}\right)e^{i\mathbf{k}\cdot\mathbf{R}} \end{aligned} \tag{1.3.6}$$

doi:10.6342/NTU201700233

Once we know the interaction terms, the equation can be written in a matrix form.

$$\begin{aligned} b_\alpha E(\mathbf{k}) &= b_\alpha \varepsilon_\alpha + \sum_{\beta} b_\beta U^{self}_{\alpha,\beta} \\ &+ \sum_{\beta,\mathbf{R}_{1st}} b_\beta U^{1^{st}}_{\alpha,\beta} e^{i\mathbf{k}\cdot\mathbf{R}_{1st}} + \sum_{\beta,\mathbf{R}_{2nd}} b_\beta U^{2^{nd}}_{\alpha,\beta} e^{i\mathbf{k}\cdot\mathbf{R}_{2nd}} + \ldots \end{aligned} \tag{1.3.7}$$

The details for calculating the interaction terms $U_{\alpha,\beta}$ were given by Slater-Koster two-center integrals [15]. For each $\mathbf{k}$ vector, we can write sown a matrix equation and sove the corresponding eigen states. In reality, we often consider terms up to 2nd nearest interaction only. Models aimimg for the III-V and IV group semiconductors have been developed by several researchers. The sp^3 first and second nearest interaction model were developed by *Chadi* and *Cohen* [16]. This model can only deal with the valence band correctly, and fail to fit the X point states. *Vogl*, *Hjalmarson*, and *Dow* [2] added an s^* orbital to the sp^3 basis to mimic the influence of the d orbital, and was successful to reproduce the conduction band minimum. However, the transverse masses at these points did not agree with experiments. Finally, the d orbital was included by *Jancu* [4]. This $sp^3d^5s^*$ model was accurate enough comparing to first principle methods and experiments, and

doi:10.6342/NTU201700233

was widely used in quantum transport simulation.

To produce those parameters, we can either calculate by the first principle method, so called the ab-initio tight binding [17], or fit the band edge values measured by experiments. Once we fit the parameters of a new material, it is easy and fast to do the calculation again, and the parameters are scalable and adjustable to apply on other situations like, for example, different boundary conditions, different amount of strains or atoms from the same group [18].

1.4 Tight Binding in Quantum Structures

Recent years, the development of Moore's law has been slowed down, for the process of scaling down planar MOSFETs met lots of difficulties. As the integrated circuit industry comes to this turning point, engineers must to investigate alternative structures and devices. Transistors with new structures like FinFET [19], nanowire FET [20], vertical nanowire FET [21], heterostructure nanowire FET [22], tunneling FET [23], or even 2D material FET [24] have been performed in the research center worldwide. In 2015, 16-nm FinFETs first showed up in our every day life with the form of smartphone CPU. Under the scaling of device dimensions, the crystal symmetry, bond orientation,

doi:10.6342/NTU201700233

and quantum confinement will matter. Our bulk tight binding model based on periodic boundary condition will need some alterations. We will take the square nanowire structure in the following as an example.

In the bulk tight binding model, the wavefunction is the linear combination of the atomic orbitals in the primitive cell atoms.

Primitive cell wavefunction:

$$\psi_{\mathbf{k}}(\mathbf{r}) = \sum_{\mathbf{R},\eta} b_\eta e^{i\mathbf{k}\cdot\mathbf{R}} \psi_\eta (\mathbf{r} - \mathbf{R}) \ , \tag{1.4.1}$$

where $\eta = s, p_x, p_y, p_z, ...$ For a square nanowire structure, the periodicity in the two directions break, so we will have to include the orbitals of all the atoms in the cross section into the base. The "supercell" wavefunction will become

Supercell wavefunction:

$$\psi_{\mathbf{K}}(\mathbf{r}) = \sum_{\mathbf{R}_{wire},l,\eta} B_{l,\eta} e^{i\mathbf{K}\cdot\mathbf{R}_{wire}} \psi_\eta (\mathbf{r} - \mathbf{R_l} - \mathbf{R}_{wire}) \ , \tag{1.4.2}$$

where l is the index describing the lth unit cells in the supercell. Thus as we construct the nanowire Tight Binding Hamiltonian, we need to take the atomic orbital energy and the interaction energy of all the atoms in the cross section into account. In this thesis we will use this model to calculate the silicon nanowire band structure.

doi:10.6342/NTU201700233

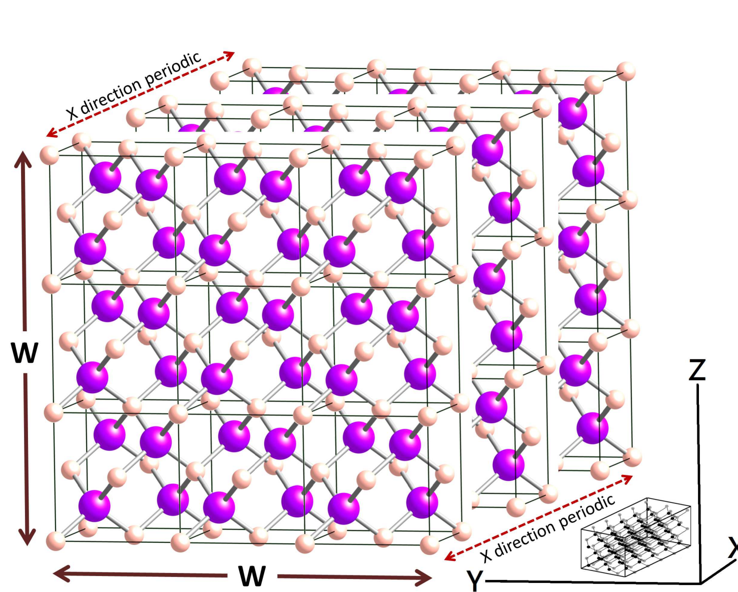

Figure 1.2: The figure shows the periodicity of a silicon nanowire. The y, z directions are confined with the confined width = W. The x direction is the transport direction with the periodic boundary condition.

1.5 Molybdenum Disulfide and its Nanoribbon

A we mentioned above, 2D materials are candidate materials for the next-generation electronic devices. However, the physics inside is still unclear. With the Tight Binding tool, we can get into details the characteristics of new 2D materials.

Transition metal dichalcogenides (TMDCs) have attracted much attentions. The monolayer is composed of a sheet of transition metals sandwiched between two sheets of chalcogen (S, Se or Te). Each layer is attracted to the other layers by van der waals force. The special 2D scheme gives them good chemical and mechanical stability.

doi:10.6342/NTU201700233

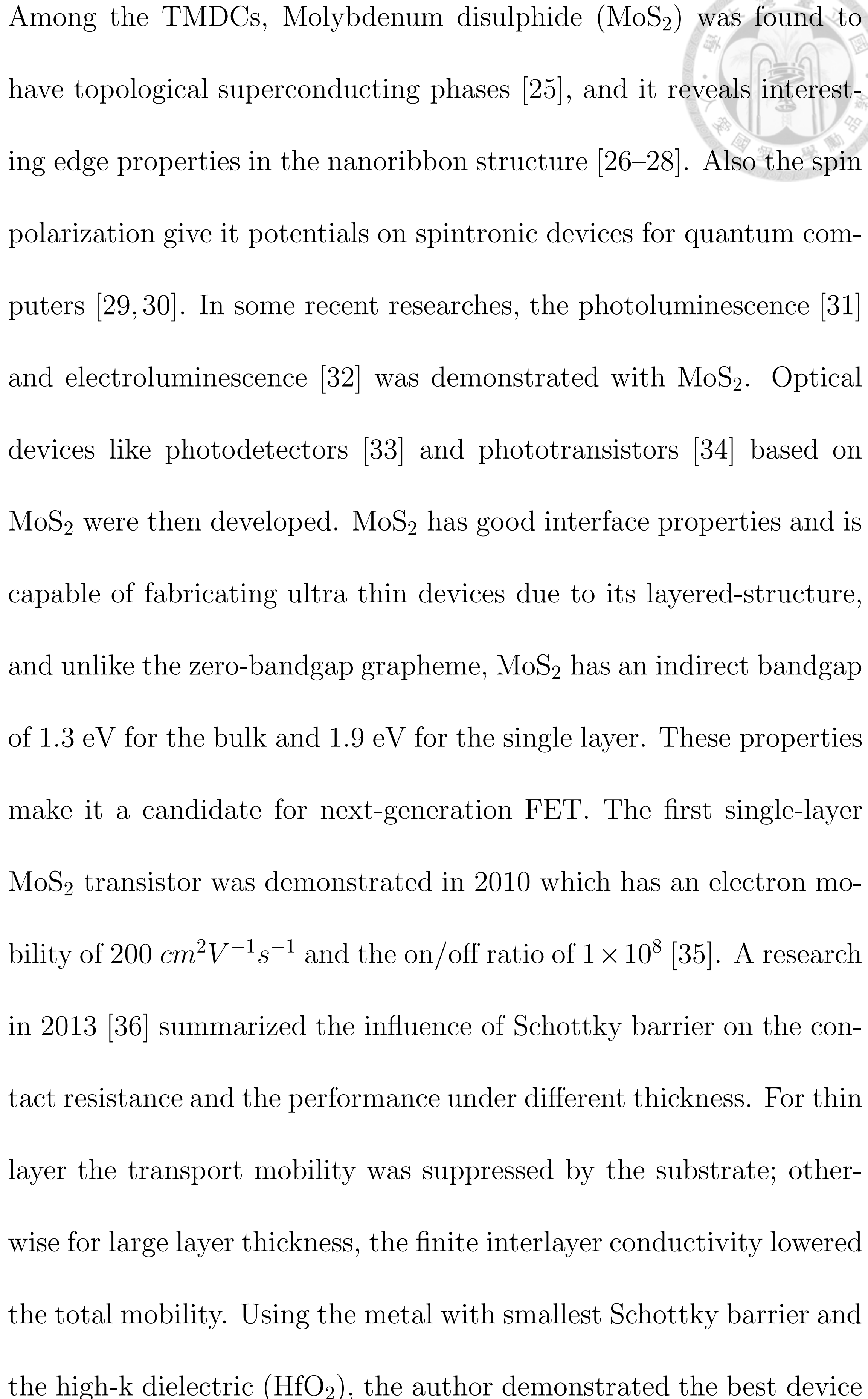

Among the TMDCs, Molybdenum disulphide (MoS_2) was found to have topological superconducting phases [25], and it reveals interesting edge properties in the nanoribbon structure [26–28]. Also the spin polarization give it potentials on spintronic devices for quantum computers [29, 30]. In some recent researches, the photoluminescence [31] and electroluminescence [32] was demonstrated with MoS_2. Optical devices like photodetectors [33] and phototransistors [34] based on MoS_2 were then developed. MoS_2 has good interface properties and is capable of fabricating ultra thin devices due to its layered-structure, and unlike the zero-bandgap grapheme, MoS_2 has an indirect bandgap of 1.3 eV for the bulk and 1.9 eV for the single layer. These properties make it a candidate for next-generation FET. The first single-layer MoS_2 transistor was demonstrated in 2010 which has an electron mobility of 200 $cm^2V^{-1}s^{-1}$ and the on/off ratio of 1×10^8 [35]. A research in 2013 [36] summarized the influence of Schottky barrier on the contact resistance and the performance under different thickness. For thin layer the transport mobility was suppressed by the substrate; otherwise for large layer thickness, the finite interlayer conductivity lowered the total mobility. Using the metal with smallest Schottky barrier and the high-k dielectric (HfO_2), the author demonstrated the best device

doi:10.6342/NTU201700233

with an electron mobility of 700 $cm^2V^{-1}s^{-1}$ and an on-state current density of 240 $\mu A/\mu m$. MoS_2 transistors may reveal potentials in

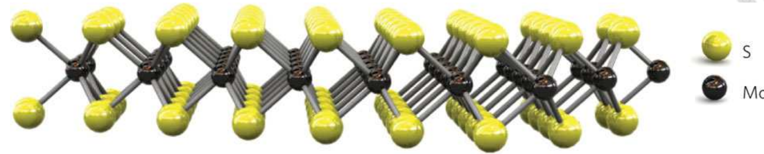

Figure 1.3: The crystal structure of a single-layer MoS_2. The figure was a copyright from [1].

next-generation devices. However, the dimensions of devices from the literatures seemed to be too large compared to those in the silicon-based integrated circuit industry. In addition, the performance still need some improvement. Therefore in this thesis, we will focus on the impacts of applying strains and under quantum confinement effect by our established tool−the quantum structure tight binding model.

doi:10.6342/NTU201700233

Chapter 2 Methodology

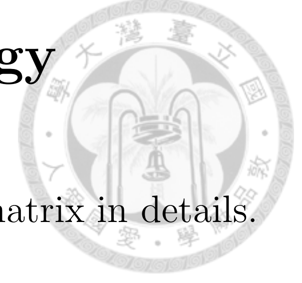

In this chapter, we will introduce the tight binding matrix in details. The contents will begin from the bulk, expending to the nanowire. Then we will show how to deal with the boundary condition and include strains into the model. In the end is the numerical methods for effective mass and density-of-states calculation.

2.1 Tight Binding Hamiltonian: Bulk

To introduce the tight binding matrix in details, we will take the bulk III-V material GaAs for example. The primitive unit cell contains two atoms. If we choose sp^3 orbitals as the base, and consider only first nearest neighbor interaction, the matrix will be of the form

$$\begin{pmatrix} E_{s,Ga} & 0 & 0 & 0 & H_{1s,2s} & H_{1s,2p_x} & H_{1s,2p_y} & H_{1s,2p_z} \\ 0 & E_{p,Ga} & 0 & 0 & H_{1p_x,2s} & H_{1p_x,2p_x} & H_{1p_x,2p_y} & H_{1p_x,2p_z} \\ 0 & 0 & E_{p,Ga} & 0 & H_{1p_y,2s} & H_{1p_y,2p_x} & H_{1p_y,2p_y} & H_{1p_y,2p_z} \\ 0 & 0 & 0 & E_{p,Ga} & H_{1p_z,2s} & H_{1p_z,2p_x} & H_{1p_z,2p_y} & H_{1p_z,2p_z} \\ H_{2s,1s} & H_{2s,1p_x} & H_{2s,1p_y} & H_{2s,1p_z} & E_{s,As} & 0 & 0 & 0 \\ H_{2p_x,1s} & H_{2p_x,1p_x} & H_{2p_x,1p_y} & H_{2p_x,1p_z} & 0 & E_{p,As} & 0 & 0 \\ H_{2p_y,1s} & H_{2p_y,1p_x} & H_{2p_y,1p_y} & H_{2p_y,1p_z} & 0 & 0 & E_{p,As} & 0 \\ H_{2p_z,1s} & H_{2p_z,1p_x} & H_{2p_z,1p_y} & H_{2p_z,1p_z} & 0 & 0 & 0 & E_{p,As} \end{pmatrix}, \tag{2.1.1}$$

doi:10.6342/NTU201700233

where index 1 represents Ga, index 2 represents As. The terms E_s, E_p are the atomic orbital steady state energy.

$H_{1\alpha,2\beta} = \langle \psi_{1,\alpha}(\mathbf{r}) \mid H \mid \psi_{2,\beta}(\mathbf{r}-\mathbf{R}) \rangle$ is the first-nearest neighbor interaction term between the α orbital of the atom 1 and the β orbital of the atom 2. From the relation $\langle \psi_{1,\alpha}(\mathbf{r}) \mid H \mid \psi_{2,\beta}(\mathbf{r}-\mathbf{R}) \rangle = \langle \psi_{2,\beta}(\mathbf{r}-\mathbf{R}) \mid H \mid \psi_{1,\alpha}(\mathbf{r}) \rangle^*$, it can be shown that the Hamiltonian is Hermitian. The first-nearest neighbor interaction term equals to

$$\begin{aligned} H_{1\alpha,2\beta} &= \langle \psi_{1,\alpha}(\mathbf{r}) \mid H \mid \psi_{2,\beta}(\mathbf{r}-\mathbf{R}) \rangle \\ &= \int d\mathbf{r} \psi^*_{1,\alpha}(\mathbf{r}) U(\mathbf{r}) \psi_{2,\beta}(\mathbf{r}-\mathbf{R}) e^{i\mathbf{k}\cdot\mathbf{R}} = U_{1\alpha,2\beta} e^{i\mathbf{k}\cdot\mathbf{R}} \end{aligned} \tag{2.1.2}$$

$U_{1\alpha,2\beta}$ is the parameter we will need. According to the atomic physics it contains the σ bonding and the π bonding parts. Fig. 2.1 gives an insight into the influence of bonding degree and bonding length on the interaction energy. For example the E_{p_x,p_x} term of a III-V material equals to $\left(\frac{1}{3}V_{pp\sigma} + \frac{2}{3}V_{pp\pi}\right) e^{i\mathbf{k}\cdot\mathbf{R}}$, where $\mathbf{R}$ is the vector between two neighbor atoms.

In the final step, we need to plus all the first-nearest-neighbor atoms to the same matrix element. Again in the III-V material example, there are four first-nearest-neighbor atoms with vectors $\mathbf{R} = \left\{\frac{a}{4}(1,1,1), \frac{a}{4}(1,-1,-1), \frac{a}{4}(-1,1,-1), \frac{a}{4}(-1,-1,1)\right\}$. Then the $H_{1s,2p_x}$

doi:10.6342/NTU201700233

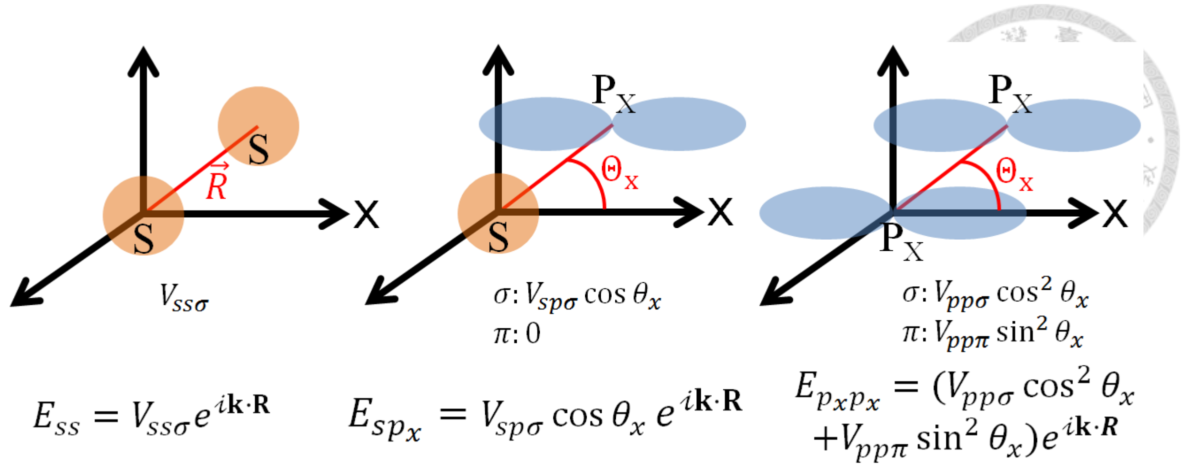

Figure 2.1: The interaction energy under different conditions. $\mathbf{R}$ isthe vector between two neighbor atoms, and θ_x is the angle between the bonding vector and the x axis.

term will be

$$H_{1s,2p_x} = \sum_{\mathbf{R}} V_{sp\sigma}\frac{\mathbf{R}\cdot\hat{a}_x}{|\mathbf{R}|}e^{i\mathbf{k}\cdot\mathbf{R}}$$

$$= \frac{V_{sp\sigma}}{\sqrt{3}}\left[e^{i\mathbf{k}\cdot\frac{a}{4}(1,1,1)} + e^{i\mathbf{k}\cdot\frac{a}{4}(1,-1,-1)} - e^{i\mathbf{k}\cdot\frac{a}{4}(-1,1,-1)} - e^{i\mathbf{k}\cdot\frac{a}{4}(-1,-1,1)}\right] \tag{2.1.3}$$

Details of other orbital interaction terms are given in [15].

2.2 Tight Binding Hamiltonian: Nanowire

As we have mentioned previously, the break of periodicity gives the nanowire Bloch wavefunction a new description

Bulk:

$$\psi_{\mathbf{k}}(\mathbf{r}) = \sum_{\mathbf{R},\eta} b_\eta e^{i\mathbf{k}\cdot\mathbf{R}}\psi_\eta(\mathbf{r}-\mathbf{R}) \ , \tag{2.2.1}$$

doi:10.6342/NTU201700233

Nanowire:

$$\psi_{\mathbf{K}}(\mathbf{r}) = \sum_{\mathbf{R}_{wire},l,\eta} B_{l,\eta} e^{i\mathbf{K}\cdot\mathbf{R}_{wire}} \psi_\eta (\mathbf{r} - \mathbf{R}_\mathbf{l} - \mathbf{R}_{wire}) \ . \tag{2.2.2}$$

In the nanowire wavefunction, there are three places we need to alter:

1. **The set of basis:** In bulk zinc-blende structure, all the primitive cells are considered the same. But in the nanowire, all the primitive cells in the same cross section are different. Therefore we need to sum over the primitive cell index l.

2. **The unit vectors:** The unit vectors of a primitive cell are

$$\vec{a}_1 = \frac{a}{2}(1,1,0) \ , \ \vec{a}_2 = \frac{a}{2}(1,0,1) \ , \ \vec{a}_3 = \frac{a}{2}(0,1,1) \ , \tag{2.2.3}$$

where a is the lattice constant. When it comes to the nanowire transporting through, for instance, [100] direction, the two unit vectors become

$$\vec{A}_1 = Na(0,1,0) \ , \ \vec{A}_2 = Na(0,0,1) \ . \tag{2.2.4}$$

Here we assumed that the wire has a width $W = N \times a$. The remained third unit cell will be along the transport direction. The shortest vector we can choose to complete the periodicity will be of the length a, so the third unit vector is

$$\vec{A}_3 = a(1,0,0) \ . \tag{2.2.5}$$

doi:10.6342/NTU201700233

3. **The reciprocal lattice:** The reciprocal primitive vectors of bulk zinc-blende semiconductors are given by

$$\vec{b}_1 = 2\pi \frac{\vec{a}_2 \times \vec{a}_3}{\vec{a}_1 \cdot \vec{a}_2 \times \vec{a}_3} = \frac{2\pi}{a}(1,1,-1)$$
$$\vec{b}_2 = 2\pi \frac{\vec{a}_3 \times \vec{a}_1}{\vec{a}_1 \cdot \vec{a}_2 \times \vec{a}_3} = \frac{2\pi}{a}(1,-1,1) \quad (2.2.6)$$
$$\vec{b}_3 = 2\pi \frac{\vec{a}_1 \times \vec{a}_2}{\vec{a}_1 \cdot \vec{a}_2 \times \vec{a}_3} = \frac{2\pi}{a}(-1,1,1) \ .$$

The concept of the wave vector comes from the periodic Bloch states. So in the nanowire, the two confined direction will not have the k-cpace. Instead, they form subbands projected at the transport direction k-vector. Therefore, the nanowire Brillioun zone is one-dimensional with the reciprocal unit vector equals to

$$\vec{B} = \frac{2\pi}{\vec{A}_3} = \frac{2\pi}{a}(1,0,0)\,. \quad (2.2.7)$$

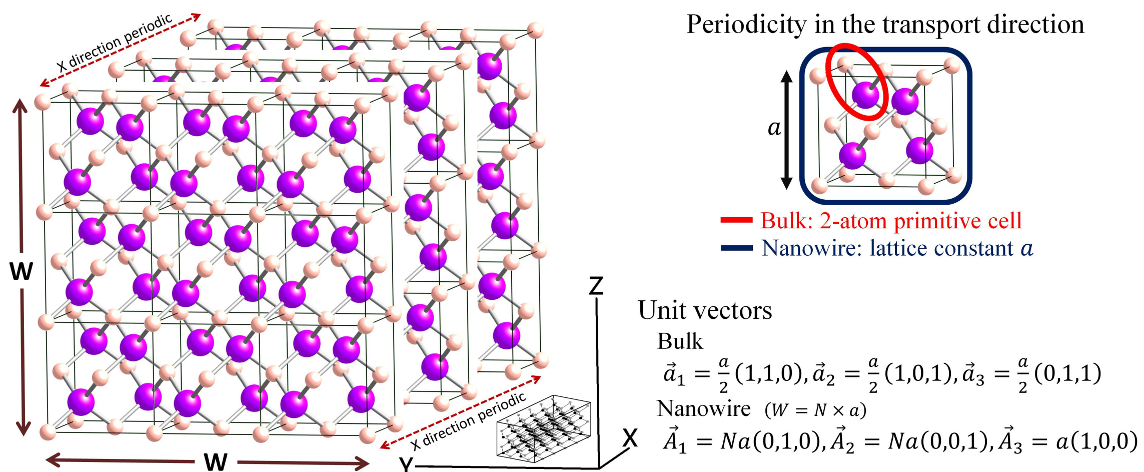

Figure 2.2: The change of periodicity makes the size and the shape of the unit cell different.

doi:10.6342/NTU201700233

2.3 Strains and Boundary Condition

In tight binding model, the interaction term is highly related to the inter-nuclear distance. The related research could be traced back to *Harrison* [37]. In this paper, interatomic matrix elements were given by a simple universal fitting approach

$$(ll'm) = \eta_{ll'm}\frac{\hbar^2}{md^2} \ . \tag{2.3.1}$$

This method was derived aiming to solve the simple sp^3 nearest-neighbor model. The fitting process was: (1)Derive the Hamiltonian for a specific structure. (fcc, bcc, ...) (2)Solve the eigen equation for some symmetric points. (3)Compare each model and figure out the parameter $\eta_{ll'm}$. Each structure has its unique $\eta_{ll'm}$ and can be applied to all the materials with the same structure. This formulas indicated the relation between the interatomic distance and the interaction energy.

$$V_{\alpha,\beta}(d) = V_{\alpha,\beta}(d_0)\left(\frac{d_0}{d}\right)^{\eta} \ , \tag{2.3.2}$$

where d_0 is the equilibrium distance, α and β are the orbitals involved. Although it was just an approximated method and is not accurate enough nowadays, the relation is still widely used in the related researches. However, since the shape of the orbital wavefunction

doi:10.6342/NTU201700233

does not really associate to the ionic position, η may not exactly equal to 2. Since then, researchers have developed different methods to fit the η parameter to improve the Si and Ge band structure calculation accuracy [38–40]. This can be a powerful tool for the tight binding model to include strains.

In the nanowire tight binding model, the bond of the surface atoms will connect to the vacancy if we do not add any extra boundary conditions. These vacancy states will form energy states within the bandgap. In reality, atoms residing on the nanowire surface will be passivated by the oxide or Hydrogen [41, 42]. The result is like filling the surface states and generating a potential barrier preventing the electrons from escaping to the vacancy. An appropriate boundary condition needs to fit the passivated atoms energy, or at least mimic the effects of those atoms. The approach was given by [43] and was briefly explained by [44]. The concept for Hydrogen-state boundary is that, we adjust the ground state orbital energy of Hydrogen (namely E_s) to be larger enough than the semiconductor orbital energy near the bandgap (often E_s), then use the relation given in Eqn. 2.3.2 to calculate the interaction terms. It can help us get rid of the surface states within the bandgap while not alter the band edge states.

doi:10.6342/NTU201700233

2.4 Effective Mass and Density of States

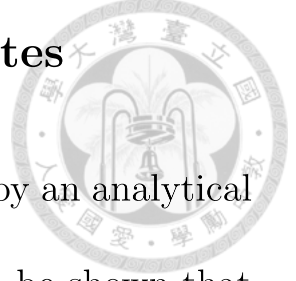

In the perfect crystal model, the E-k relation is given by an analytical form $E(k) = \hbar^2 k^2 / 2m^*$. From this assumption, it can be shown that the effective mass is equal to the free-electron effective mass and the density-of-states is equal to

$$D_{1D,anal}(E) = \frac{1}{\hbar\pi}\sqrt{\frac{2m^*}{(E - E_C)}} \tag{2.4.1}$$

However, the actual E-k relation derived from the eigen equation $H(\mathbf{k})\psi(\mathbf{k}) = E\psi(\mathbf{k})$ has no analytical form. We should calculate the effective mass and the density-of-state by definition, and apply the finite difference method.

Effective mass:

$$\begin{aligned} m^* &= \hbar^2 \left(\frac{d^2 E(k)}{dk^2} \right)^{-1} \\ &= \hbar^2 \frac{\Delta k^2}{\mid E(k+\Delta k) - 2E(k) + E(k-\Delta k) \mid} \end{aligned} \tag{2.4.2}$$

Density of state:

$$\begin{aligned} D_{1D}(E) &= \frac{1}{L}\frac{dN}{dE} = \frac{1}{L}\frac{dN}{dk}\frac{dk}{dE} = \frac{1}{L}\frac{L}{2\pi}\frac{dk}{dE} \\ &= \frac{1}{2\pi}\frac{2\Delta k}{\mid E(k+\Delta k) - E(k-\Delta k) \mid} \end{aligned} \tag{2.4.3}$$

Take the state degeneracy and the spin into account, we can get the full-band density-of-states.

doi:10.6342/NTU201700233

Chapter 3 Silicon

This chapter covers the band structure of bulk silicon and silicon nanowires. The nanowire band structure reveals the quantum confinement effect and the band folding issue. In the end of this chapter, we will investigate external potential to the bandgap and subbands splitting.

3.1 Bulk Silicon

In the beginning, we will try to construct the best Hamiltonian basis for studying the Si material. In the previous sections, we have derived the bulk Hamiltonian and introduced the development of the tight binding model. Pervious study using the empirical pseudopotential method (EPM) has been performed to analyze the percentage decomposition of different orbital wave functions [45]. It indicated that the X valley and the L valley are highly depending on the d orbital. it has also been mentioned in *Jancu* [4] that the d orbital and the s^* orbital are necessary to calculate the full band correctly. Fig. 3.1 shows the results of different models. The $sp^3d^5s^*$ first-nearest-neighbor model is widely used since it can fit the energy states and the effective mass

doi:10.6342/NTU201700233

near the band edges well. In the later sections, we will apply this model in the following nanowire calculation.

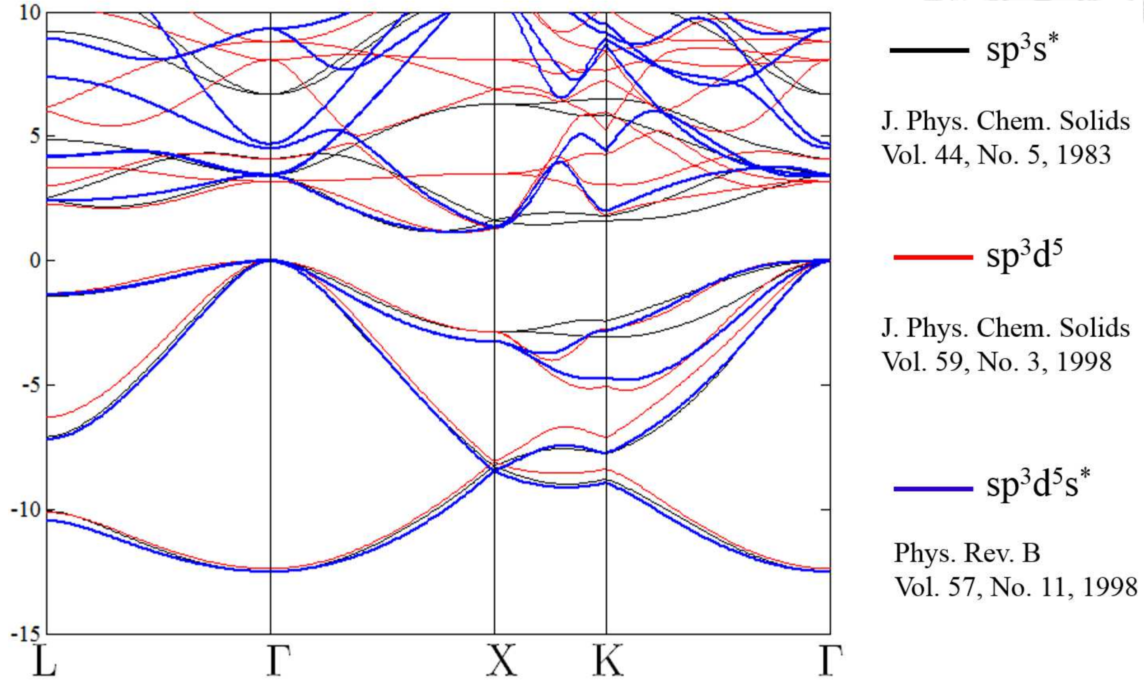

Figure 3.1: Bulk silicon band structures with sp^3s^* [2], sp^3d^5 [3] and $sp^3d^5s^*$ [4] orbital basis respectively.

3.2 Silicon Slab and Surface States

Before getting to the nanowire calculation, we would like to demonstrate some quantum slab results. Quantum slab is a kind of 2D structure with only one direction confined, as Fig. 3.2 shows. In the section 2.3 we have mentioned that surface atoms will form dangling bond states if we do not apply any boundary condition. Fig. 3.3 shows the 5.5 nm thick quantum slab with and without hydrogen pas-

doi:10.6342/NTU201700233

sivation. The case without hydrogen passivation shows some obvious surface states.

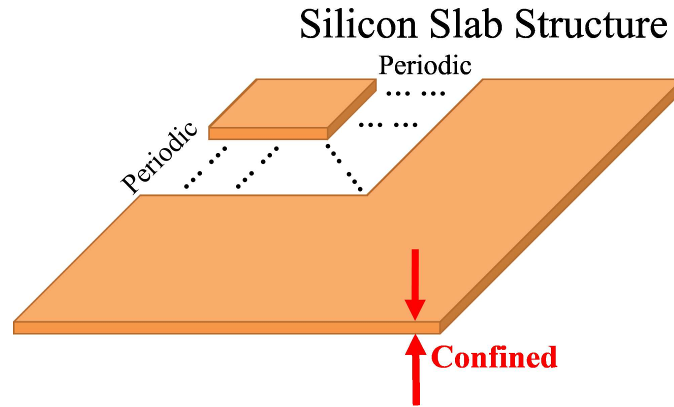

Figure 3.2: Quantum slab structure. The plane is large enough to be treated as infinite.

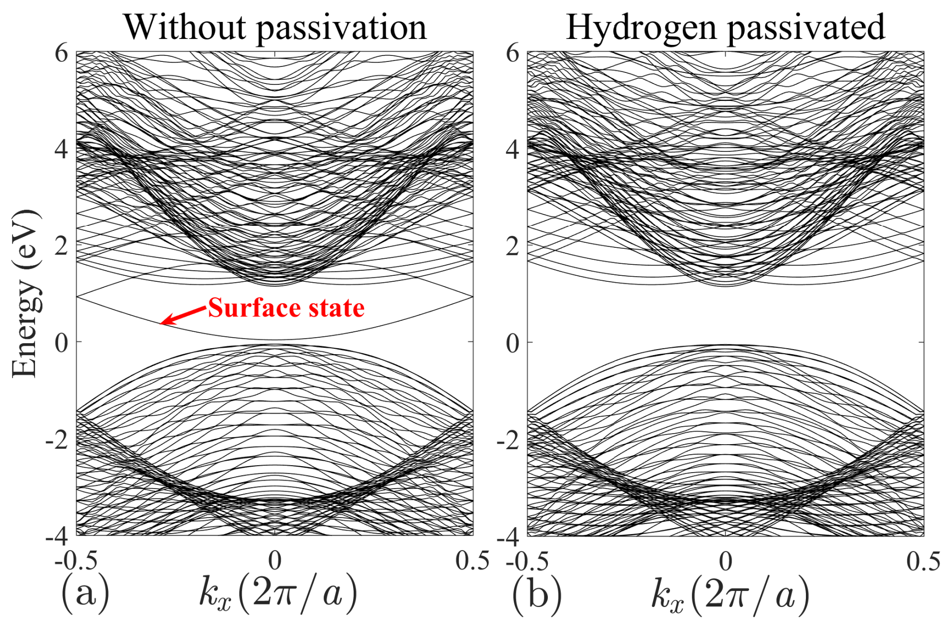

Figure 3.3: 5.5 nm thick quantum slab without surface passivation and with hydrogen passivation.

doi:10.6342/NTU201700233

3.3 Silicon Nanowire

In this section, we will present the silicon nanowire band structures along the [100] direction. The structure profile was shown in Fig. 2.2. Four layers of atoms are necessary to complete the one-dimensional periodicity. Surface atoms are passivated by increasing the dangling-bond energy and adding hydrogen-like atoms with only s orbital. Considering the first-nearest-neighbor $sp^3d^5s^*$ model with the cross section atom number equals to N, the boundary atom number equals to N_H, and take into account the boundary hydrogen atoms, the ultimate matrix size will be $(10 \times N + N_H)$. Details have been discussed in the methodology section.

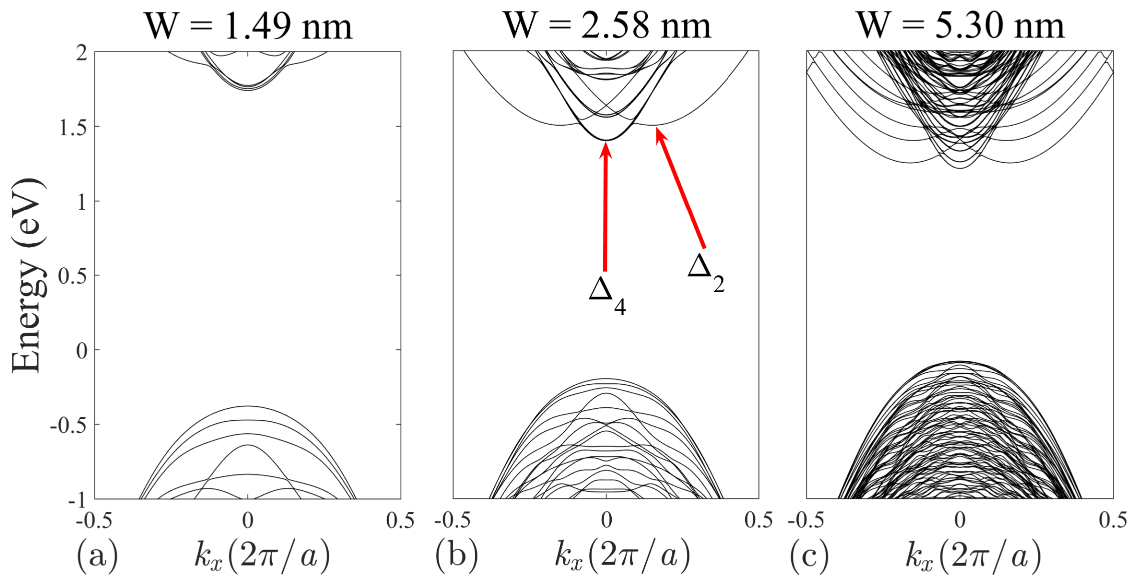

Figure 3.4: Silicon nanowire [100] band structure with (a) W = 1.49 nm, (b) W = 2.58 nm and (c) W = 5.30 nm.

doi:10.6342/NTU201700233

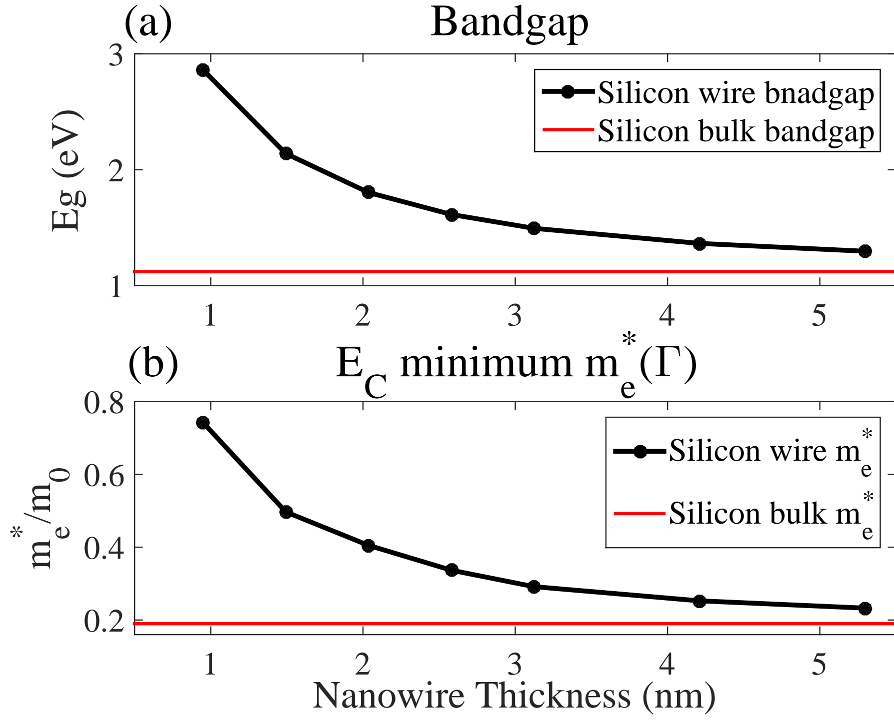

Figure 3.5: Silicon nanowire band gap and conduction band edge effective mass (Γ point) versus the wire width. a is the lattice constant.

Fig. 3.4 shows the band diagram of [100] direction silicon nanowire with W = 1.49 nm, W = 2.58 nm and W = 5.30 nm. The bandgap and the electron effective mass near the Γ valley under different wire width are shown in Fig. 3.5. The effective mass was calculated by Eqn. 2.4.2. According to the quantum confinement effect, the bandgap broadening is roughly equal to

$$\Delta E_g = \frac{\pi^2\hbar^2}{2m_e^{*2}W^2} + \frac{\pi^2\hbar^2}{2m_h^{*2}W^2} \propto \frac{1}{W^2} \tag{3.3.1}$$

However, in real cases, the effective mass also increases with the dimension scaling, so the bandgap will magnify more seriously than the

doi:10.6342/NTU201700233

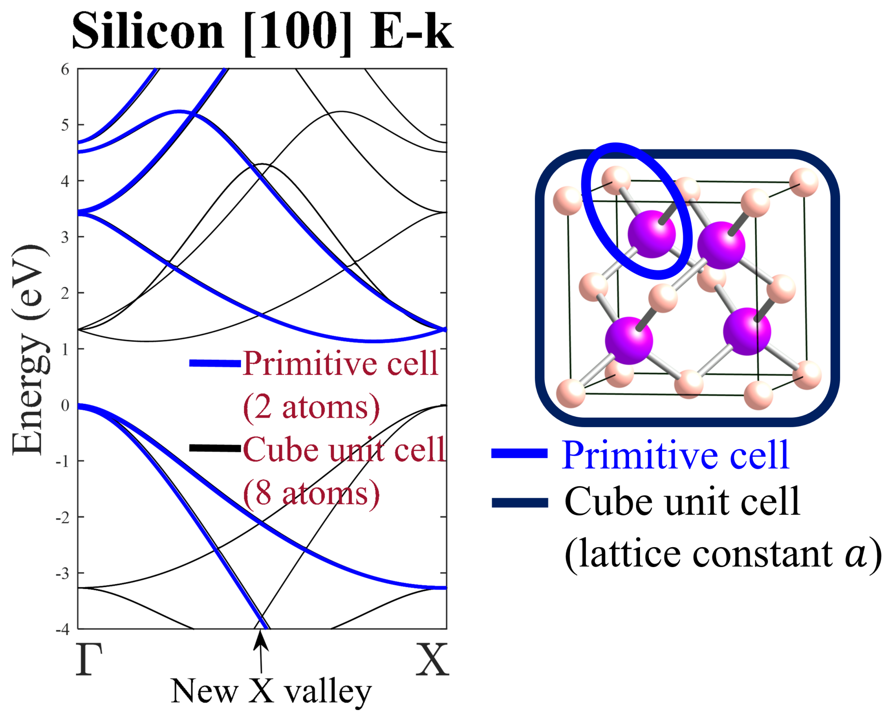

Figure 3.6: [100] direction band structure calculated by the primitive unit cell (2 atoms) and the cube unit cell (8 atoms).

semi-classical prediction. We can see that for a thicker wire, m_e^* is close to the bulk value ($0.19m_0$). The properties will be more like the bulk.

It is known that the bulk silicon has an indirect bandgap. However, Fig. 3.4 indicates that the silicon nanowire has a direct bandgap. This is the result of band folding. We have explained in the section 2.2 that the first Brillouin zone will shrink when the unit cell enlarges. As a result, the states with a large wavevector will fold back to the first Brillouin zone as shown in Fig. 3.4. To find the wavevectors of the folded states, we need to compare the Brillouin zone (BZ) of the two

doi:10.6342/NTU201700233

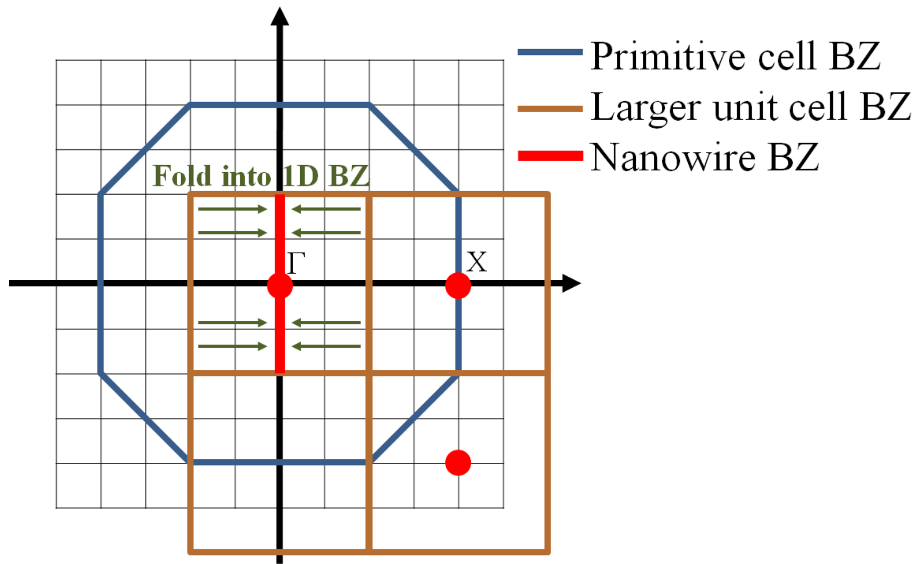

Figure 3.7: 2D projection of the first Brillouin zone (BZ). The blue line is the primitive unit cell BZ, while the brown line is the cube unit cell BZ.

unit cells. The 2D projection of the Brillouin zone (BZ) in Fig. 3.7 gives us some clues. The blue line is the primitive unit cell BZ, while the brown line is the cube unit cell BZ. To fill the primitive first Brillouin zone, four unit cells are needed. So the Γ valley of the large cell will contain the states at the positions of the three red dots. We can apply this method to find the folded states at other symmetric points. Also, schemes to unfold all the states systematically have been performed. It can be shown that those folded states are the superposition of the original states [46–48].

The concept of the band folding can now be applied to the nanowire

doi:10.6342/NTU201700233

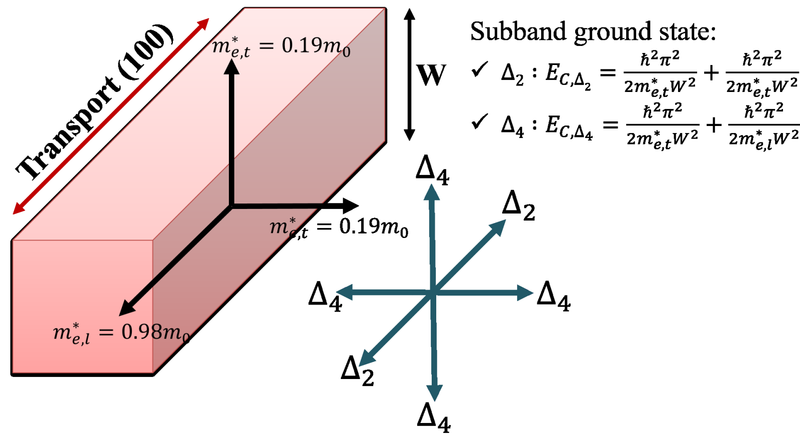

Figure 3.8: The difference of the transverse effective ($0.19m_0$) and the longitudinal effective mass ($0.98m_0$) for silicon makes the density-of-state effective mass at the six X valleys different.

band structure. For the transport direction, four layers of atoms are necessary for the nanowire tight binding calculation, which makes the unit cell two times longer than the primitive cell. As a result, the first BZ will be half of the original BZ, and the X valley will fold back to the Γ point. For the other two confined directions, the periodicity breaks and all the states will fold into the 1D k-space, forming the dense subbands shown in Fig. 3.4. The subbands splitting can be approximated as $\pi^2\hbar^2/2m^{*2}W^2$ in the simple infinite quantum wire model, while our results with corrected effective mass are more accurate. Therefore, a smaller wire will have a larger subband splitting.

Another feature we can observe in Fig. 3.4 is the conduction band minimum splitting. For a bulk silicon, the conduction band minimum

doi:10.6342/NTU201700233

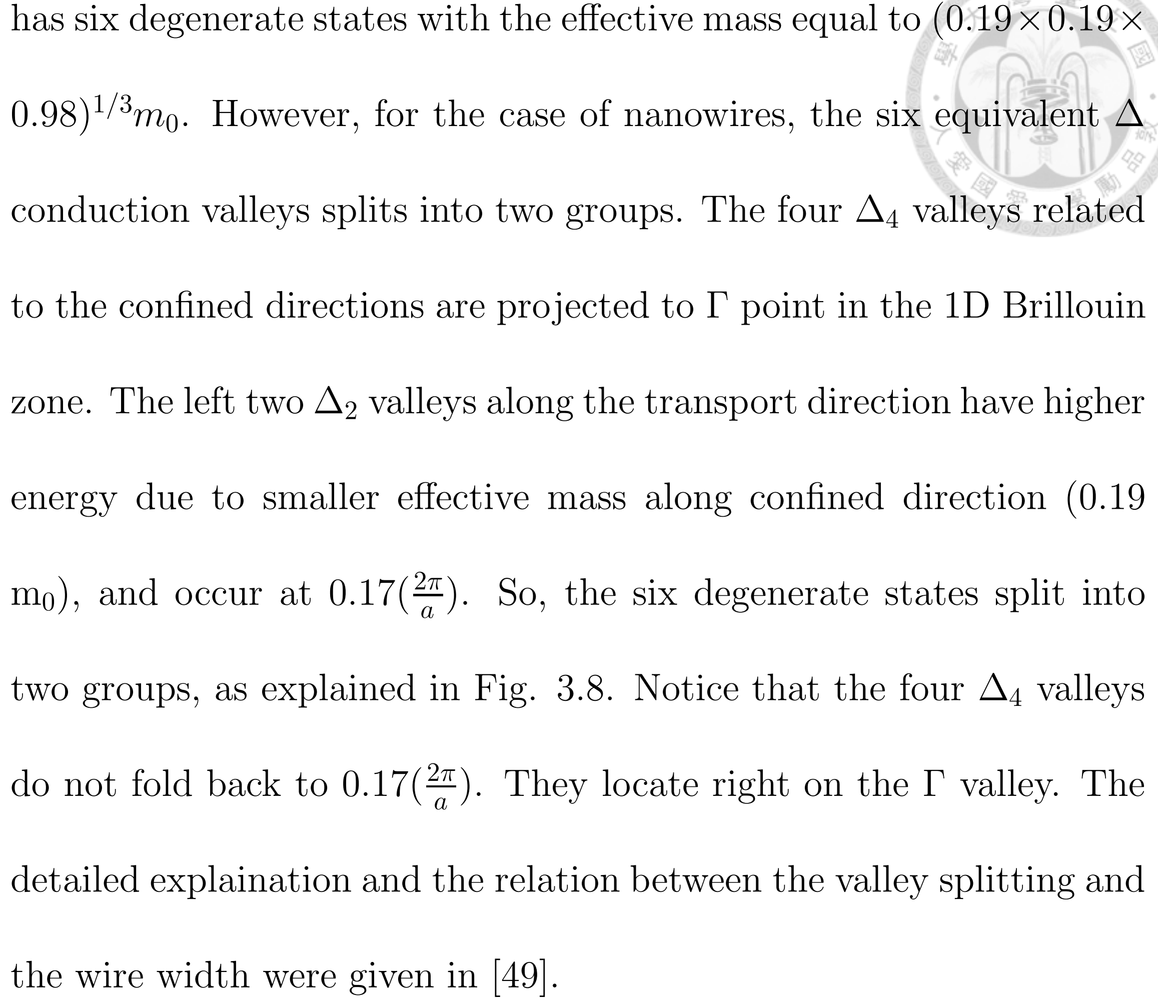

has six degenerate states with the effective mass equal to $(0.19 \times 0.19 \times 0.98)^{1/3} m_0$. However, for the case of nanowires, the six equivalent Δ conduction valleys splits into two groups. The four Δ_4 valleys related to the confined directions are projected to Γ point in the 1D Brillouin zone. The left two Δ_2 valleys along the transport direction have higher energy due to smaller effective mass along confined direction (0.19 m$_0$), and occur at $0.17(\frac{2\pi}{a})$. So, the six degenerate states split into two groups, as explained in Fig. 3.8. Notice that the four Δ_4 valleys do not fold back to $0.17(\frac{2\pi}{a})$. They locate right on the Γ valley. The detailed explaination and the relation between the valley splitting and the wire width were given in [49].

3.4 Band Structure under External Potential

In the real nanowire MOSFET device,the wire will be covered by a layer of oxide. Outside the oxide is the metal contact with an applied gate voltage. To mimic the gate voltage effect, we added an extra potential on the wire cross section. According the the derivation of tight binding method, the off-diagonal terms in the Hamiltonian are related to the interaction energy from different orbitals. We can assume that the external bias only affects on the diagonal term. This method was

doi:10.6342/NTU201700233

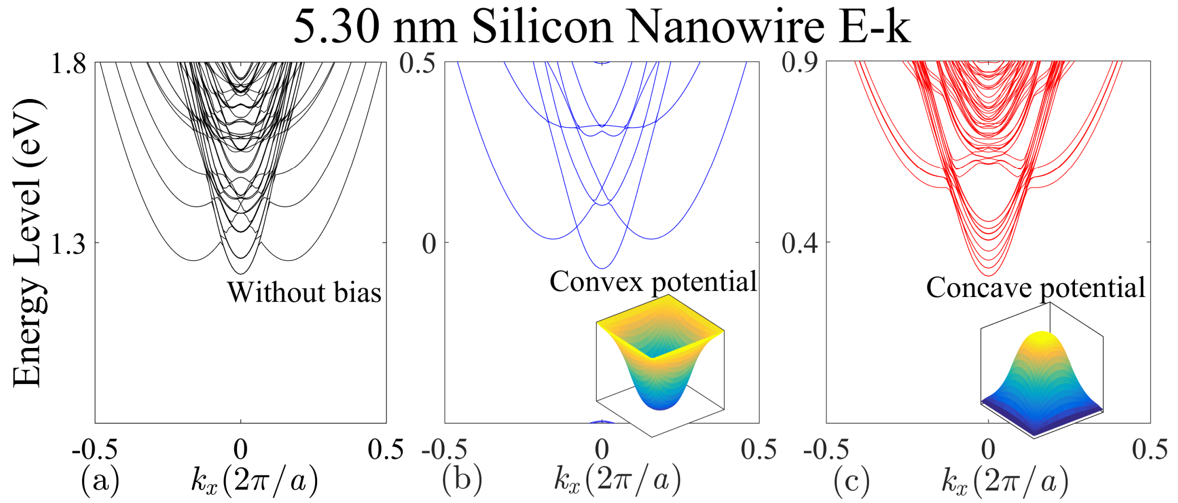

Figure 3.9: 5.30 nm wide Silicon nanowire band structure (a) without bias, (b) with convex potential, and (c) with concave potential.

applied in early studies [50].

Fig. 3.9 shows the band structure of 5.30 nm width nanowire with two kinds of nununiform curved potential. From both cases, the electrons gather in low conduction band energy positions. The effective bandgap reduces due to the quantum confined stark effect, as we showed in Fig. 3.10.

Also we observed that the separation between Δ_4 valley and Δ_2 valley enlarges in both cases. The distance between subbands at the same valley also increases. And in the case of the concave potential, the degenerate states split.

Finally in Fig. 3.12, we demonstrated how the external potential changes the carrier distribution. We plotted the conduction band min-

doi:10.6342/NTU201700233

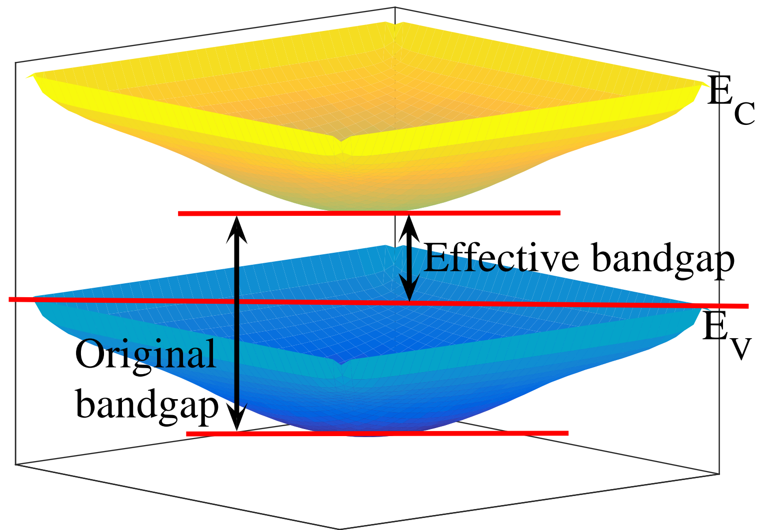

Figure 3.10: An extra potential distributed in the wire cross section will reduce the effective bandgap. It is associated to the Quantum Confinement Stark Effect.

imum wavefunction square along the wire cross section direction. The result shows that a convex potential gathers electrons, while a concave potential drives electrons to the near surface. This meets our common sense. In a nanowire MOSFET device, we apply a gate voltage to drive the electrons to the oxide-semiconductor interface. The influence of a concave potential is just the same as a gate voltage.

doi:10.6342/NTU201700233

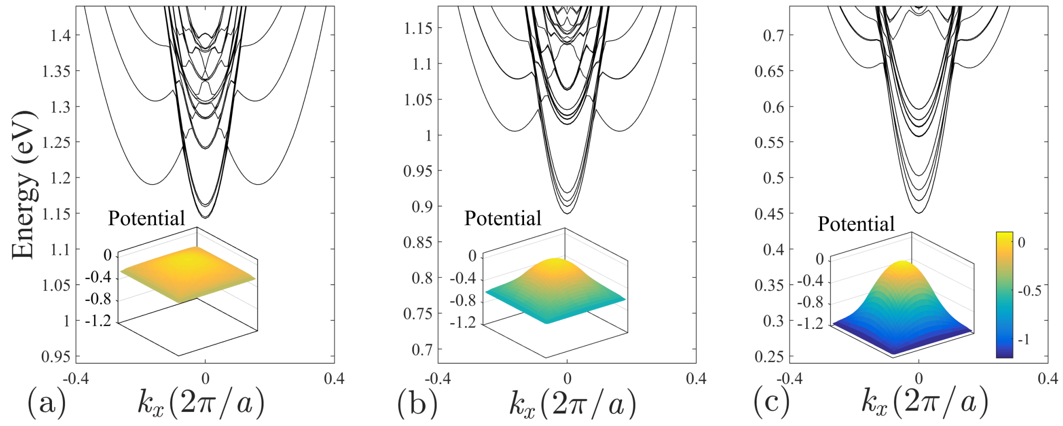

Figure 3.11: 5.30 nm wide Silicon nanowire band structure with different magnitudes of concave potentials.

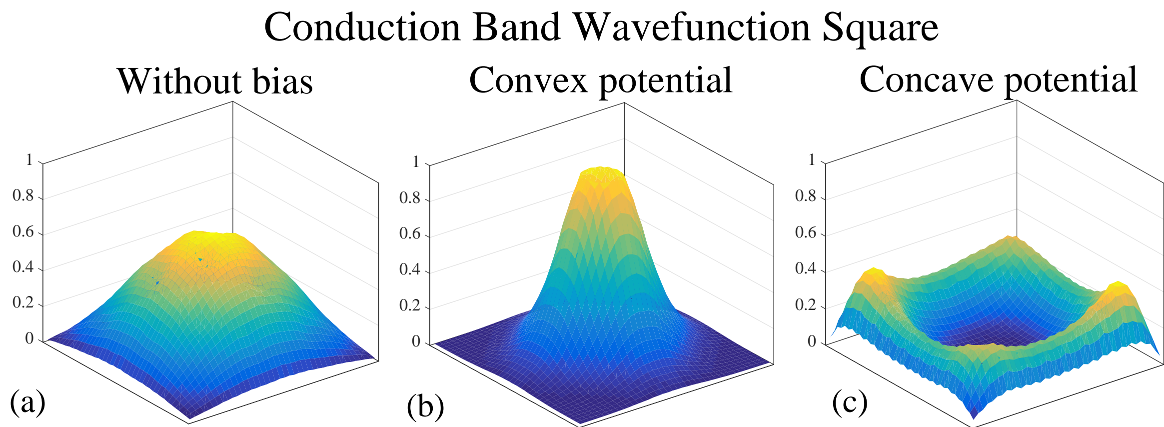

Figure 3.12: 5.30 nm wide Silicon nanowire conduction band electron wavefunction square (a) without bias, (b) with convex potential, and (c) with concave potential.

doi:10.6342/NTU201700233

Chapter 4 MoS_2

In the section 1.5, we have introduced the properties and applications of MoS_2. In this section, we will calculate the band structures of single-layer and multi-layer MoS_2 then will apply the model to study the effects of the quantum confinement and strains.

4.1 MoS_2 Tight Binding Model

Studies related to MoS_2 tight binding calculation are still in development. The earliest one has just been published in 2013 [51], where they used the generic algorithm to violently fit the density functional theory. To fit the full-band correctly in a wide range of energies, they chose non-orthogonal first-nearest Mo(sp^3d^5), S(sp^3d^5) orbitals as the basis. Usually we choose orthogonal basis for fitting and treat these base as orbital wavefunctions. But, in reality, these orbital wavefunctions are overlapping and are not orthogonal. Applying the overlap integral, the Schrödinger equation becomes a generalized eigenvalue problem

$$\mathbf{H}\psi_k = (\mathbf{1} + \mathbf{S})\psi_k E \ , \tag{4.1.1}$$

doi:10.6342/NTU201700233

where

$$S_{\mu,\nu} = \int \psi_\mu(r)\psi_\nu(r)\,dr - \delta_{\mu,\nu} \; . \tag{4.1.2}$$

In this model, they also included the spin-orbit coupling since the spin-orbit-induced spin splitting in two-dimensional transition-metal dichalcogenide semiconductors is large [52]. This model gave an excellent fitting result. However, the fitting process was time-demanding and was lack of physical conceptions. Therefore, scientists tried to simplify the model by using the smallest basis with only necessary orbitals. A research also published in 2013 [53] analyzed the orbital compositions of the generalized-gradient approximation (GGA) result near the band edge. The author summarized that the wavefunctions are dominated mostly by d orbitals of Mo atoms, especially d_{z^2}, d_{xy} and $d_{x^2-y^2}$ orbitals. The results considering only first-nearest nighbor atoms could fit only the band edge. After taking third-nearest neighbor atoms into accounts, they successfully fitted the band in full k-space. The three-band model was simple, and the orbital characteristics were rather clear. The disadvantages were obvious−three bands were not enough to further analyze the properties. The band structure was lack of too many energy states. To improve the model, a recent research published in 2015 [54] included the p orbitals of S atoms and

doi:10.6342/NTU201700233

the d_{yz}, d_{xz} orbitals of Mo atoms into the basis, totally 11 components. The author chose the DFT-HSE06 band structure [55] as a reference for their fitting. The fitted result was in consistent with the DFT ones. We summarized the three models in Fig. 4.1. Notice that the bandgap

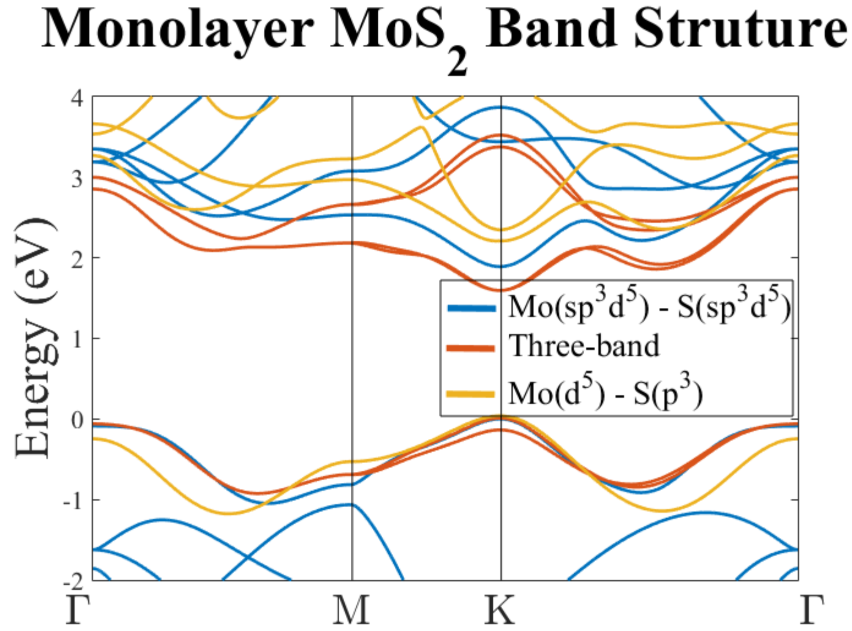

Figure 4.1: Monolayer MoS_2 band structure with different models from reference.

predicted by the three models are different. The difference is due to the different first-principle reference they chose. It is known that the traditional DFT functionals based on the local density approximation (LDA) and on the generalized gradient approximation (GGA) underestimate the bandgap [56–58]. The reason is that the exciton binding energy of MoS_2 is quite large, making the electronic bandgap differs a lot from the optical bandgap (1.88 eV) measured by photolumines-

doi:10.6342/NTU201700233

cence. However, the exciton binding energy measured or calculated by different researches [59–62] were different ($0.6\ eV - 0.9\ eV$). Further researches on this novel material is necessary to confirm its properties.

In the following sections, we will apply the non-orthogonal first-nearest sp^3d^5 model [51] on the study of strains and nanostructures. When the structure of a material changes, the orbital composition and the energy state position in the band structure will also change. Therefore, a model containing a large enough basis is necessary. Although this model is more complicated, containing non-orthogonal basis, and was fitted by a process lack of physical conceptions, it contains enough orbital informations. So it is the best model for nanostructure researches.

4.2 Strain Effects

As we mentioned previously, the transistor devices fabricated by MoS_2 suffer from low mobility. In the industry, engineers have been adopting strains on silicon to improve its mobility. Strained silicon can be easily fulfilled by growing Si-Ge alloy. As for MoS_2, the processes to apply strains were difficult and still in development due to its 2D structure. One popular method is to grow MoS_2 on a suitable substrate, than

doi:10.6342/NTU201700233

give the substrate an external compressive stress. The MoS_2 sheet on top of the substrate will form a wrinkled structure with strains [5]. Nevertheless, a reproducible and stable process is still unavailable. Also the physics behind strained MoS_2 still needs further researches.

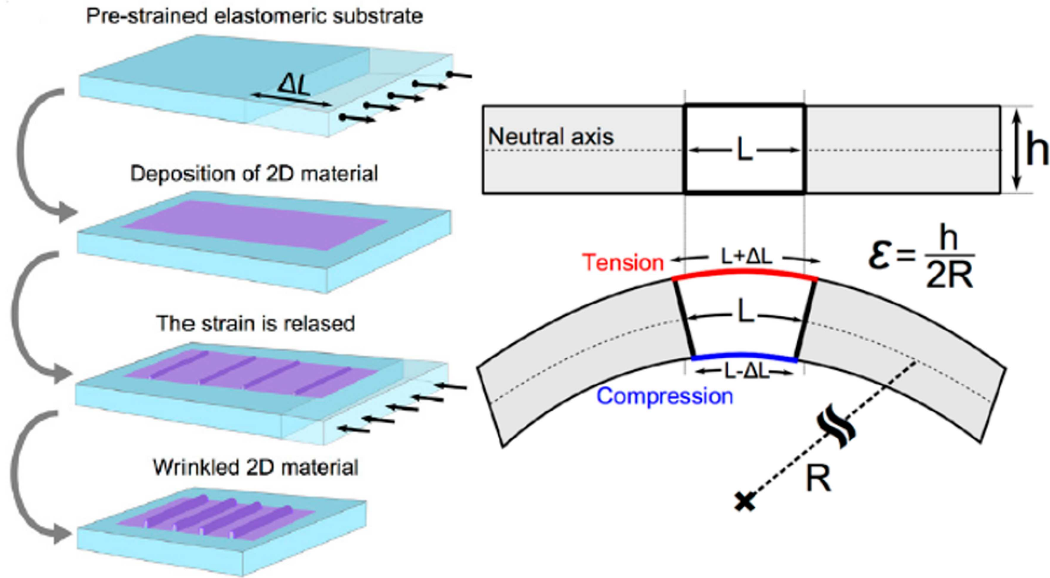

Figure 4.2: To apply strains in MoS_2, engineers grow MoS_2 on the substrate then give the substrate a compressive strain [5].

Due to Poisson contraction effect, the two S-atom planes will become closer with an in-plane tension. Meanwhile, an in-plane tensile strain applied in one direction (uniaxial strain) will compress the atoms in the other direction. We found the in-plane and the out-of-plane Poisson's ratio from the literature [63]

$$\sigma_{\parallel} = -\frac{\epsilon'_{yy}}{\epsilon_{xx}} = -\frac{\epsilon'_{xx}}{\epsilon_{yy}} = 0.21 \tag{4.2.1}$$

$$\sigma_{\perp} = -\frac{\epsilon'_{zz}}{\epsilon_{xx}} = -\frac{\epsilon'_{zz}}{\epsilon_{yy}} = 0.27\ . \tag{4.2.2}$$

doi:10.6342/NTU201700233

In this section, we will include the strain effect into the tight binding model according to the theory introduced in section 2.3 with the given Poisson's ratio.

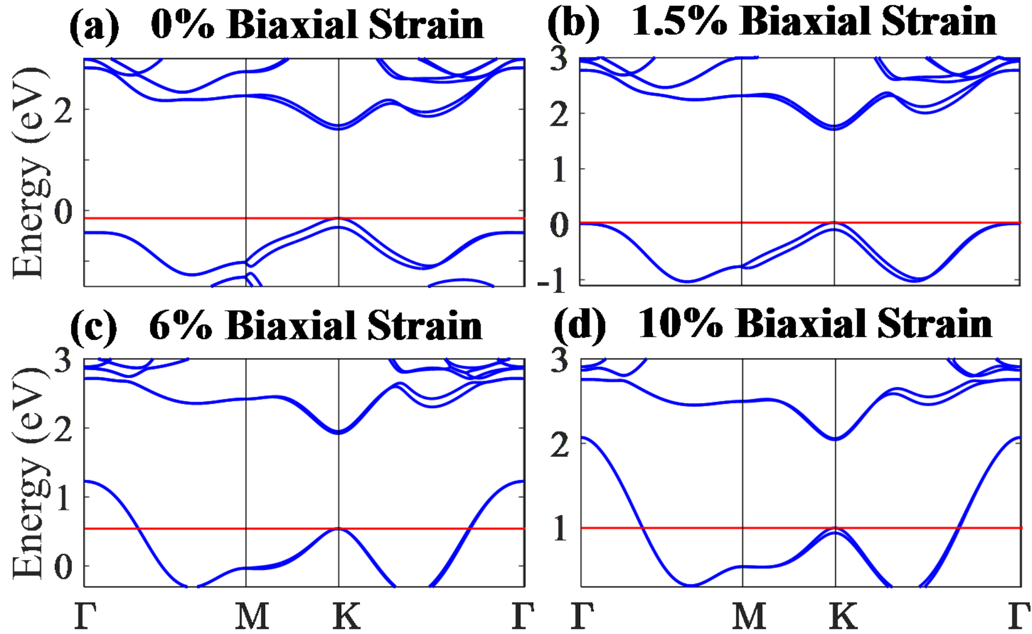

Figure 4.3: Monolayer MoS_2 under (a) 0%, (b) 1.5%, (c) 6% and (d) 10% biaxial strains on the X-Y lateral plane.

First, we added an uniform tentile strain in the in-plane direction, so called the "biaxial" strain, which means we give a strain in both x and y direction with the same magnitude. Fig. 4.3 shows the band structure calculation results. Before applying the biaxial tensile strains, MoS_2 has a direct bandgap at the K valley. The valence band energy becomes larger with an increasing tensile strain. The Γ valley rises faster than the K valley, and finally exceeds the K valley with the biaxial tensile strain larger than 1.5%. The material bandgap be-

doi:10.6342/NTU201700233

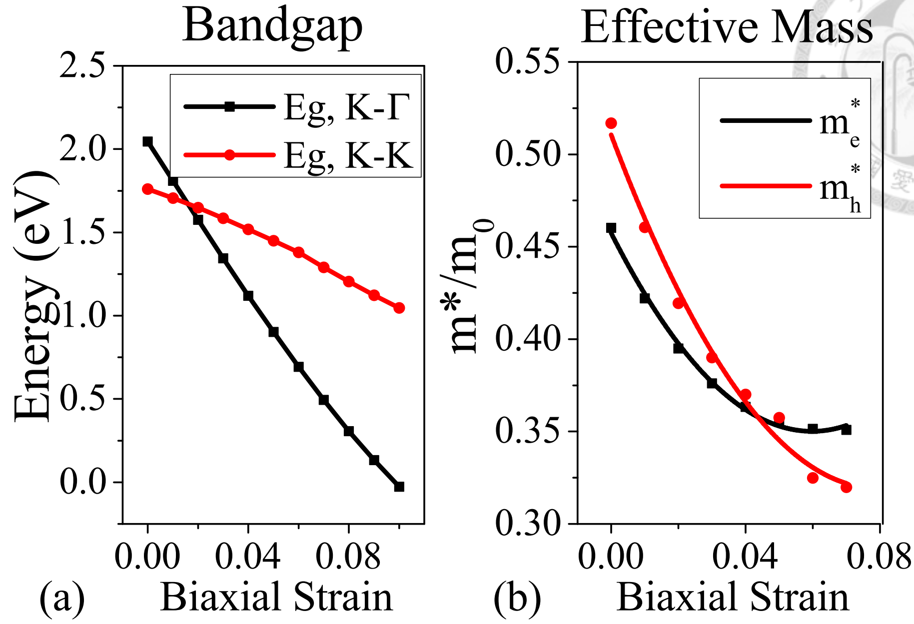

Figure 4.4: (a) The K-K direct bandgap and the K-Γ indirect bandgap under different biaxial strains. (b) The carrier effective mass at K valley under different biaxial strains.

comes indirect. We applied the strains up to the maximum MoS_2 can endure−12% [64]. In our calculation, when the biaxial tensile strain is larger than 10%, the valence band maximum touches the conduction minimum. The material becomes metallic.

With the electronic band structure, we can figure out the bandgap and the effective mass. The relation between the bandgap and the biaxial strains is shown in Fig. 4.4 (a). The bandgap is roughly inversely proportional to the biaxial strain. A direct-to-indirect bandgap transition happens at 1.5% biaxial strain. Fig. 4.4 (b) shows the carrier effective mass at the K valley along K-to-Γ direction. The electron

doi:10.6342/NTU201700233

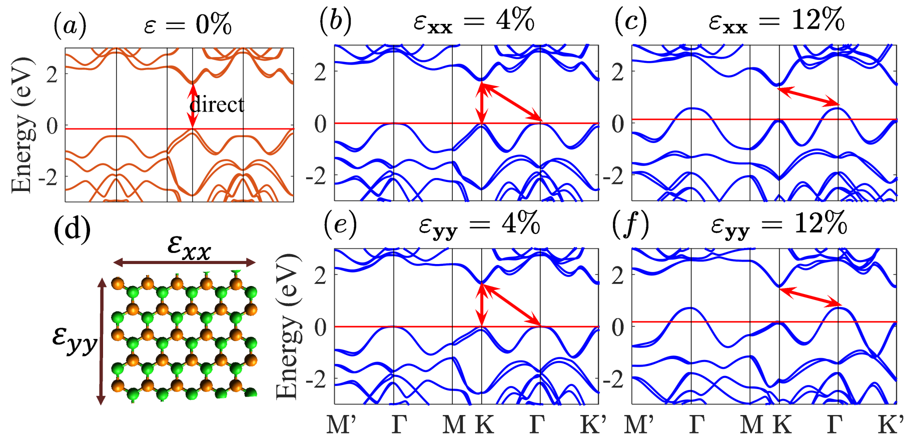

Figure 4.5: Monolayer MoS_2 band structures (a) without strains, with (b) 4%, (c) 12% tensile strains at x directions, and (f) 4%, (g) 12% tensile strains at y directions. (d) Structure profile.

effective mass and the hole effective mass both decrease as the biaxial strain increases with a similar trend.

Next, a tensile strain is added in only one in-plane direction, which is called "uniaxial" strain. The other in-plane direction will feel a compressive strain. The vertical direction will be compressed as well. The compressive ratio can be calculated by Poisson's ratio (Eqn. 4.1.3, Eqn. 4.1.4). Fig. 4.5 shows the results. Here y direction is equivalent to the Mo-S bond direction, whereas x direction is 30 degree away from the Mo-S bond. With an uniaxial strain larger than 4% for both x and y direction, the direct bandgap exceeds the indirect bandgap. Unlike the biaxial strain, a uniaxial strain of 12% does not close down the bandgap.

doi:10.6342/NTU201700233

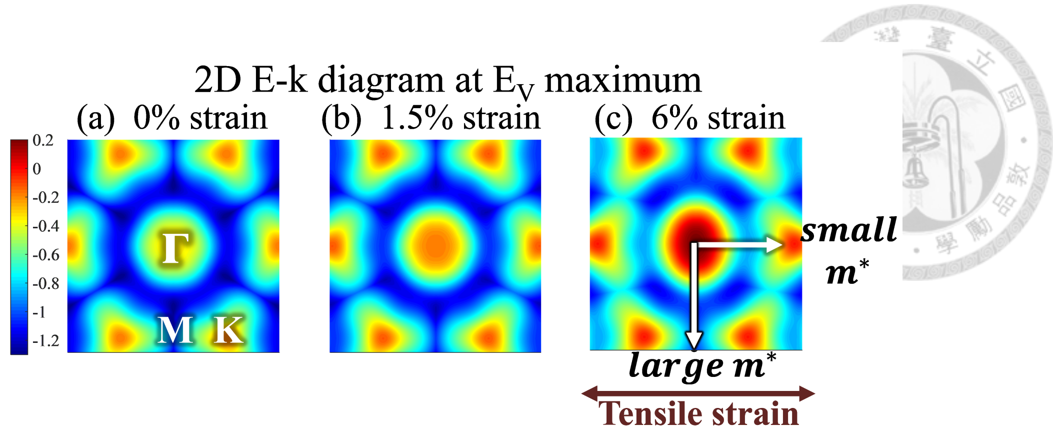

Figure 4.6: 2D E-k diagram at the valence band maximum with (a) 0%, (b) 1.5% and (c) 6% uniaxial tensile strains. The direction is shown in the brown double arrow.

Before calculating the effective mass, we plotted the 2D band structure of the valence band maximum state (Fig. 4.6). The deformations on the shape of the band structure by the uniaxial tensile strain is inhomogeneous. The direction with a tensile strain in the real space will be compressive in the k-space. We can intuitively assume the effective mass along the tensile strain direction to be smaller when the strain increases. Our calculations of the effective mass will focus on the direction along the tensile strain and along Γ to K valley.

The relation between the bandgap and the uniaxial strains is shown in Fig. 4.7 (a). The bandgap is roughly inversely proportional to the uniaxial strain. A direct-to-indirect bandgap transition happens at 4% uniaxial tensile strain. The effect is similar to the previous case

doi:10.6342/NTU201700233

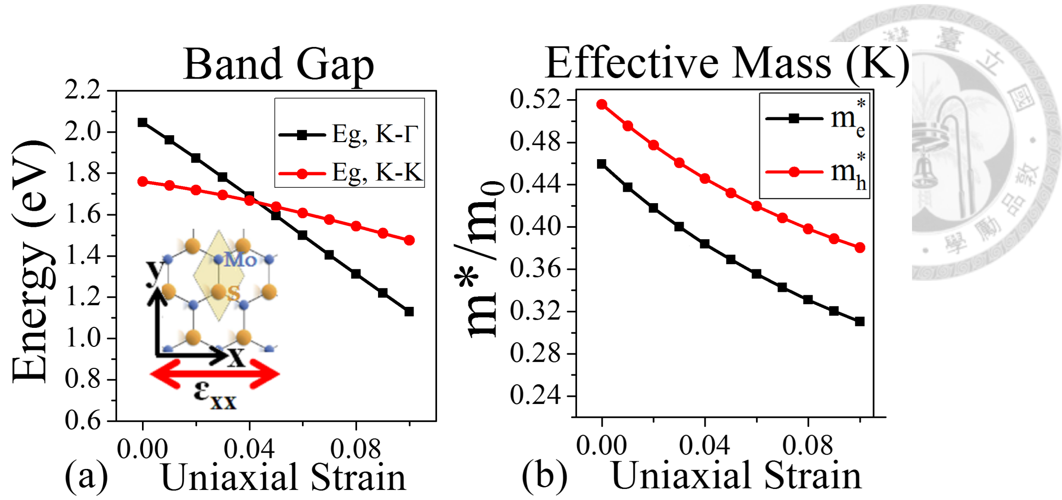

Figure 4.7: (a) The K-K direct bandgap and the K-Γ indirect bandgap under different uniaxial strains. (b) The carrier effective mass at K valley under different uniaxial strains.

with biaxial strains, whereas the magnitude of strains causing direct-to-indirect bandgap transition is larger. Fig. 4.7 (b) shows the carrier effective mass at K valley along the strain direction. In this case, we applied the uniaxial tensile strain along the x direction, and calculated the effective mass along the x direction as well. The electron effective mass and the hole effective mass both decrease with increasing uniaxial tensile strains. The trend is similar to the biaxial strain.

From the bulk MoS_2 calculation, we have indicated that the direct-to-indirect bandgap transition happens when the tensile strain reaches a critical value. Therefore, the dominated hole effective mass is actually at Γ valley under large strain conditions. Fig. 4.8 shows the hole effective mass under tensile strains at the Γ valley. Fig. 4.8 (a)

doi:10.6342/NTU201700233

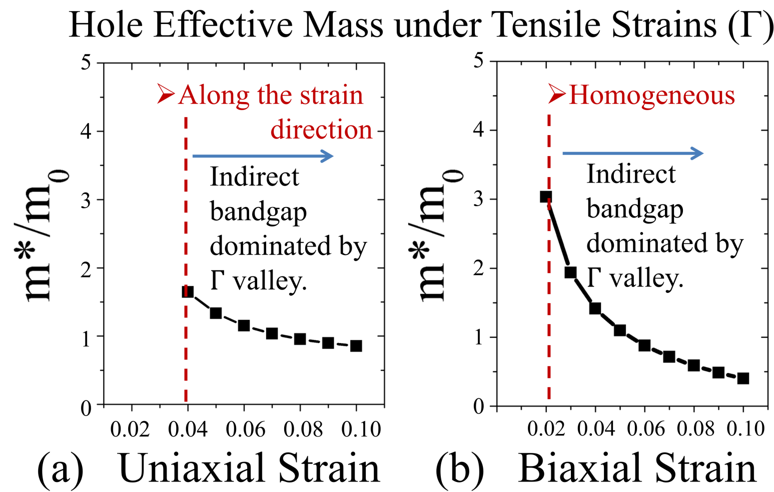

Figure 4.8: The hole effective mass at Γ valley along Γ to K valley direction with different (a) uniaxial tensile strains (also along Γ to K direction) and (b) biaxial tensile strains. Note that for strain smaller than the red dash line, the effective mass is decided by K valley so we don't list the effective mass of Γ valley

is the Γ valley hole effective mass along the x direction with applied uniaxial tensile strains along the same direction. Fig. 4.8 (b) is the Γ valley hole effective mass with applied biaxial tensile strains. The magnitudes for both cases are obviously much larger than those at the K valley. It can be summarized from the calculation results that although the badngap and the carrier effective mass both decrease with increasing strains, the hole effective mass suddenly jump up after the critical strain (4% for uniaxial strain, 6% for biaxial strain) is reached. When the strain is larger than this critical point, the Γ valley dominates and the mobility of hole could drop significantly. The

doi:10.6342/NTU201700233

continuous improvement with increasing tensile strains is only on the electron transport.

4.3 MoS_2 Nanoribbon

As MoS_2 devices scale down, the quantum confinement effect may affect their performance. Also the influence from edge atoms becomes more obvious. In this chapter, we will study how the properties of MoS_2 change when reaching nano scales.

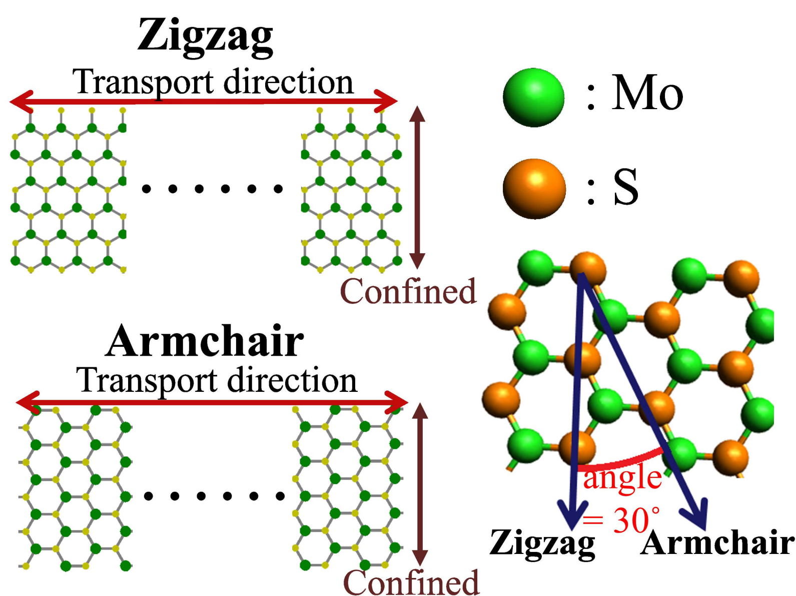

Figure 4.9: Structures of the zigzag nanoribbon and the armchair nanoribbon.

The nano structure of MoS_2 is called "nanoribbon" (NR). There are two kinds of MoS_2 nanoribbon, transporting through different direction. The armchair nanoribbon (ANR) transports through the Mo-S

doi:10.6342/NTU201700233

bond, while the zigzag nanoribbon (ZNR) transports through the Mo-Mo (or S-S) atom array. The angle between these two directions is 30 or 90 degrees. The orthogonal direction will be confined and terminated by Mo or S atoms (Fig. 4.9). Researches have been done to examine the terminated atoms [65–67]. It was reported that under hydrodesulfurization conditions, S-terminated edges become more stable. Our calculation will focus on the more controllable S-terminated NR.

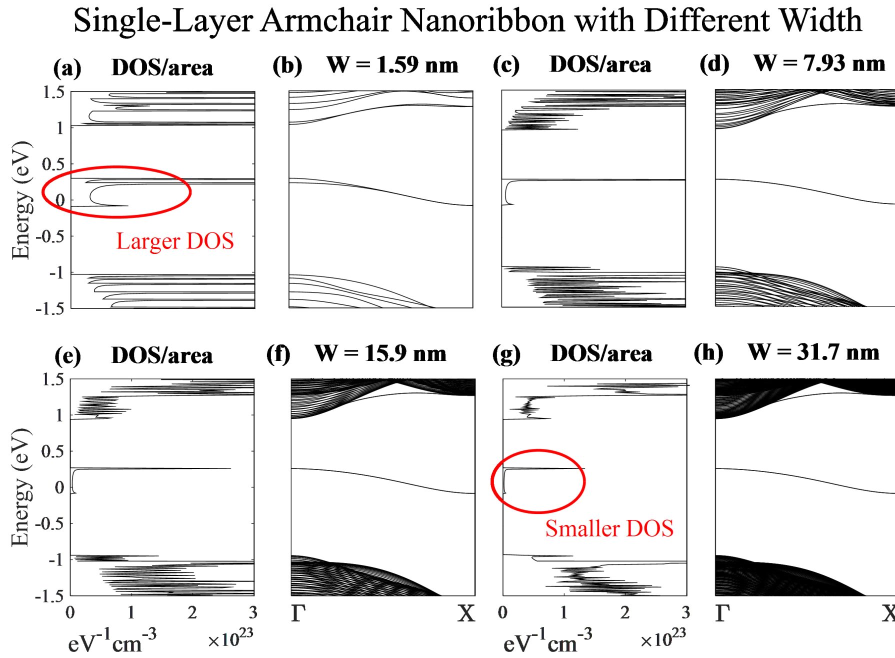

Figure 4.10: The MoS_2 armchair nanoribbon density-of-state per area with the widths equal to (a) 1.59 nm, (c) 7.93 nm, (e) 15.9 nm, (g) 31.7 nm, and the band structures with the widths equal to (b) 1.59 nm, (d) 7.93 nm, (f) 15.9 nm, (h)31.7 nm. The inset shows the structure of the armchair nanoribbon.

ANR band structures with different widths are shown in Fig. 4.10.

doi:10.6342/NTU201700233

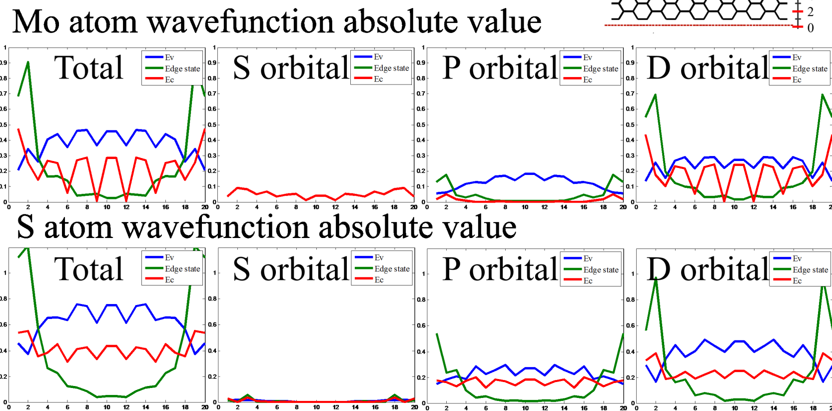

Figure 4.11: Wavefunction absolute value versus the atom position.

We also calculated the density-of-state by the method discussed in the methodology. From Fig. 4.10, we can see that the subbands become denser with an increasing width. It is reasonable because the subbands splitting is approximated inversely proportional to the square of the width according to the infinite quantum well model. However, the density-of-state per volume remains in the same order, which means that the current density won't change a lot. One surprising feature is that an intermediate state appears between the bandgap. The density-of-state of this state is larger when the width is the smaller.

To examine the intermediate state property, we analyzed the wavefunction absolute value versus the atom position. We found that the intermediate state wavefunction absolute value is largest near the edge

doi:10.6342/NTU201700233

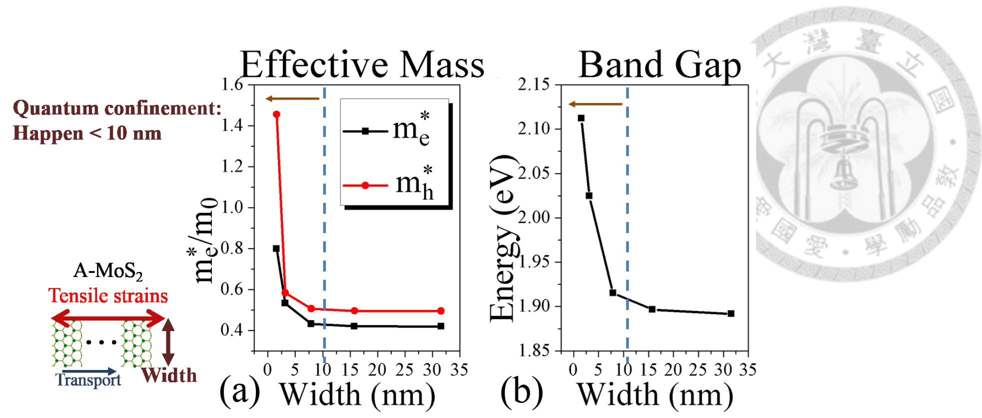

Figure 4.12: (a) The carrier effective mass and (b) the bandgap with different nanoribbon width.

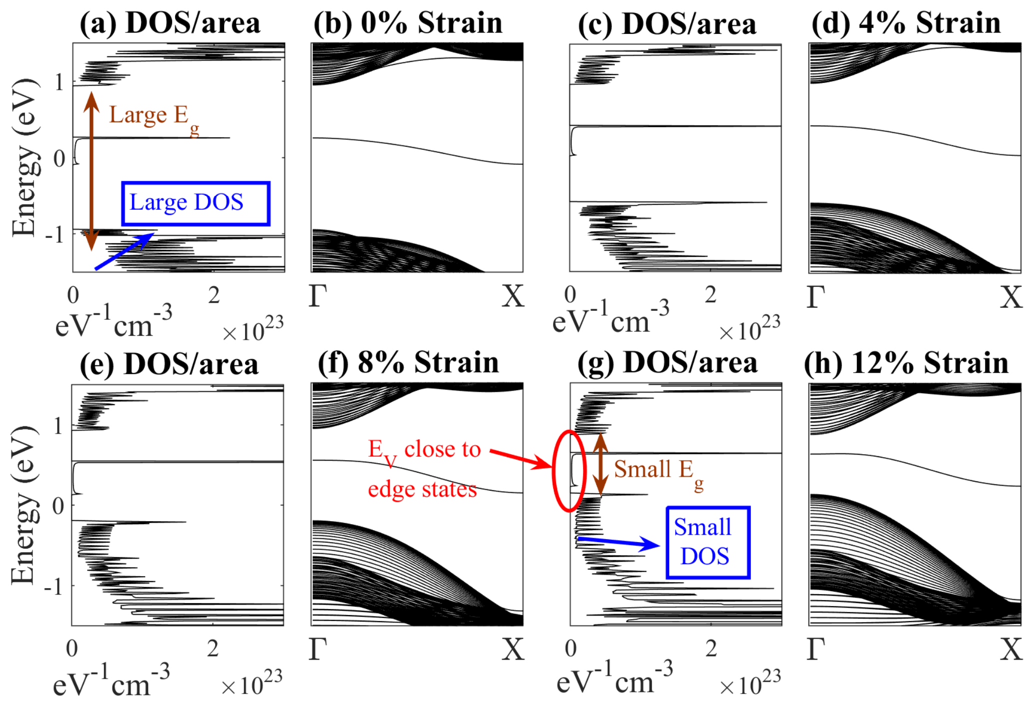

Figure 4.13: The MoS_2 armchair nanoribbon density-of-state per area with the uniaxial tensile strains equal to (a) 0%, (c) 4%, (e) 8%, (g) 12%. The band structures with tensile strains equal to (b) 0%, (d) 4%, (f) 8%, (h) 12%. The nanoribbon width is 31.7 nm. The strain is applied along the transport direction.

atoms. So, we can conclude that the intermediate band is mainly formed by edge atoms.

doi:10.6342/NTU201700233

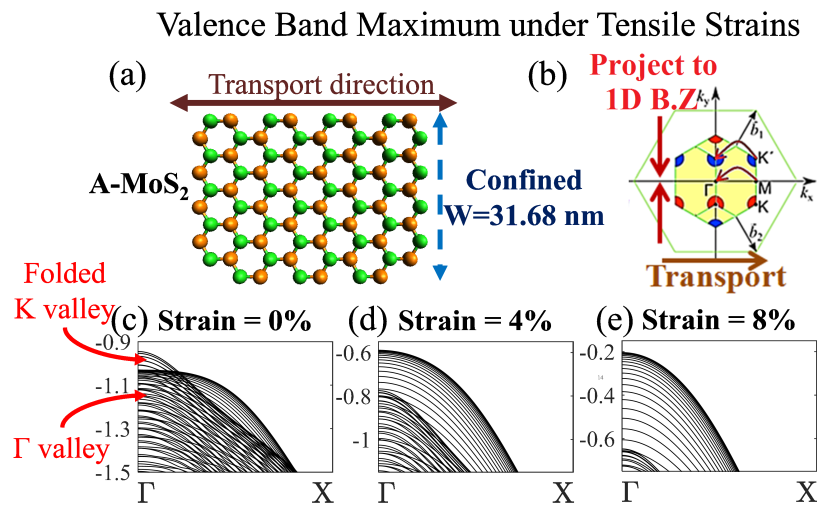

Figure 4.14: (a) Sructure profile. (b) Figure explaining the band folding issue. (c) Valence band mzximum under 0%, (d) 4% and (e) 8% tensile strains.

Fig. 4.12 summarizes the properties under different width. When the device scales down to 10 nm, the carrier effective mass and the bandgap suddenly increase, which can be explained by the quantum confinement effect. Since the hole effective mass at the K valley is smaller then the one at the Γ valley, the K valley will drop more quickly than the Γ valley. At the width smaller than 2 nm, the Γ valley dominates so the hole effective mass suddenly increases.

Afterward, we add a tensile strain along the ANR transport direction and see the effects. The E-k diagram and the density-of-state (divided by area) of a 31.7 nm width nanoribbon are plotted in Fig. 4.13. When the applied strain increases, the bandgap decreases. However, the valence band density-of-state near the band edge becomes smaller.

doi:10.6342/NTU201700233

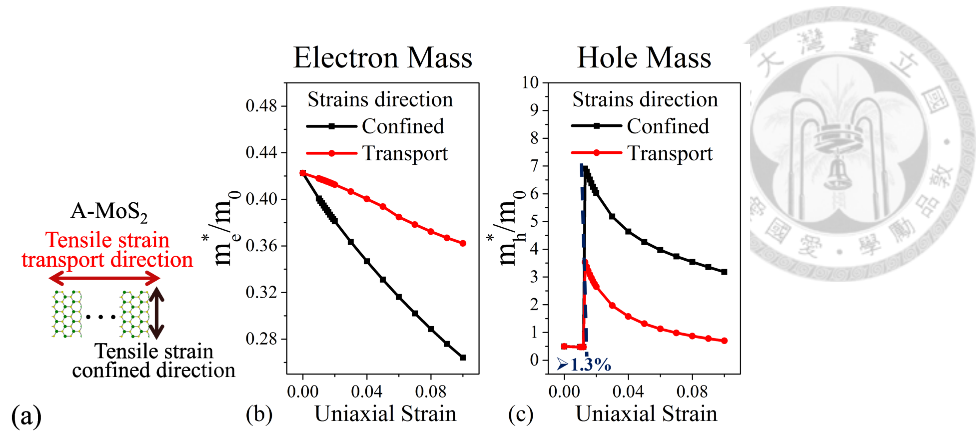

Figure 4.15: (a) Structure profile. (b) Electron effective mass and (c) hole effective mass with two different directions of strains.

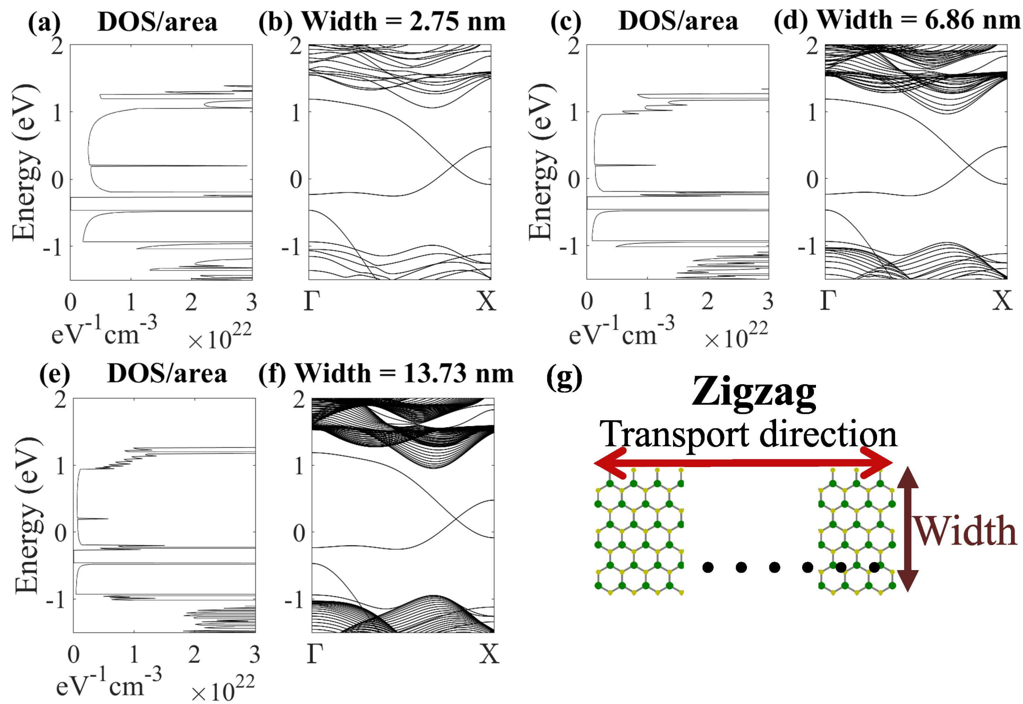

Figure 4.16: The density-of-state per area of zigzag nanoribbon with the width equal to (a) 2.75 nm, (c) 6.86 nm, (e) 13.73 nm, and the band structures with nanoribbon width equal to (b) 2.75 nm, (d) 6.86 nm, (f) 13.73 nm. (g) The zigzag structure.

Also from the density-of-state, we found that the edge state density-of-state does not change with increasing strains. It is reasonable since the edge atom concentration does not change at all. At 12% strains,

doi:10.6342/NTU201700233

the valence band maximum is really close to the edge state minimum at X valley. It will significantly affect the properties.

We know that monolayer MoS_2 becomes indirect bandgap with a large strain. But, for the nanoribbon structure, it always has a direct bandgap at Γ valley. This can be explained by the band folding issue. States at K valley and M valley will all fold into Γ valley to form mixing bands. From Fig. 4.14 we can see that the original Γ valley states rise faster than the folded K valley states, and finally dominate the valence band properties with its large hole effective mass.

In Fig. 4.15, we show the effective mass with the applied tensile strains both orthogonal and perpendicular to the transport direction. The red lines correspond to the tensile strain along the transport direction, while the black line correspond to the tensile strain perpendicular to the transport direction. Both of these strains can reduce the carrier effective mass. From the previous discussion, we know that when the tensile strain is along the confined direction, the transport direction will feel a compressive strain, and stretch the k-space, which may result in a larger effective mass. However, the rearrangement of atoms under any kinds of strains actually alters the shape of the band structure. As a result, the tensile strain along the both directions reduce

doi:10.6342/NTU201700233

the carrier effective mass.

For the other transport direction, zigzag direction, the calculation results will be totally different. Fig. 4.16 shows the results. The intermediate states now spread over the bandgap across the Fermi level. It makes the zigzag nanoribbon metal-like. Those intermediate states are formed by the edge atoms as well. So for this direction, carriers can be injected into the bulk region by the edge atoms. Same as the armchair nanoribbon, the edge-state density-of-state is largest when the ribbon width is shortest. So the carrier injection from the edge atoms can be enhanced by narrowing the nanoribbon. We have published the results above in [68].

4.4 Multi-Layer MoS_2

It is known that MoS_2 connects to each layer by van der Waals force. In tight binding method, we can simply add an interaction term and some fitted parameters to describe the interlayer characteristics. Our calculation for multi-layer MoS_2 band structures are shown in Fig. 4.17. MoS_2 changes from direct bandgap to indirect bandgap with only two layers. The bandgap of six-layer MoS_2 already approaches the bulk. Notice that the energy states for bulk MoS_2 should be

doi:10.6342/NTU201700233

distributed in the 3-D k-space, so we can see many subbands in six-layer MoS_2 band structure, but not for bulk. Finally in Fig. 4.18,

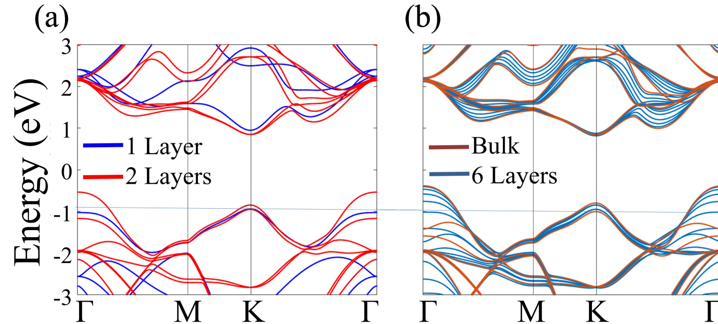

Figure 4.17: (a) Single-layer and double-layer MoS_2 band structures. (b) Six-layer MoS_2 and bulk MoS_2 band structures.

we show the density-of-state and the E-k diagrams of monolayer and five-layer nanoribbon with both ANR and ZNR. For ANR, the result is similar to the strain effect, where the bandgap shrinks as well as the valence band density-of-state. More edge states appear since there are more edge atoms for a thicker ribbon, while the density-of-state does not change a lot. For ZNR, more layers of atoms form more states within the bandgap. The difference between the conduction band and the valence band become more unclear. It may help to enhance its metal-like properties.

doi:10.6342/NTU201700233

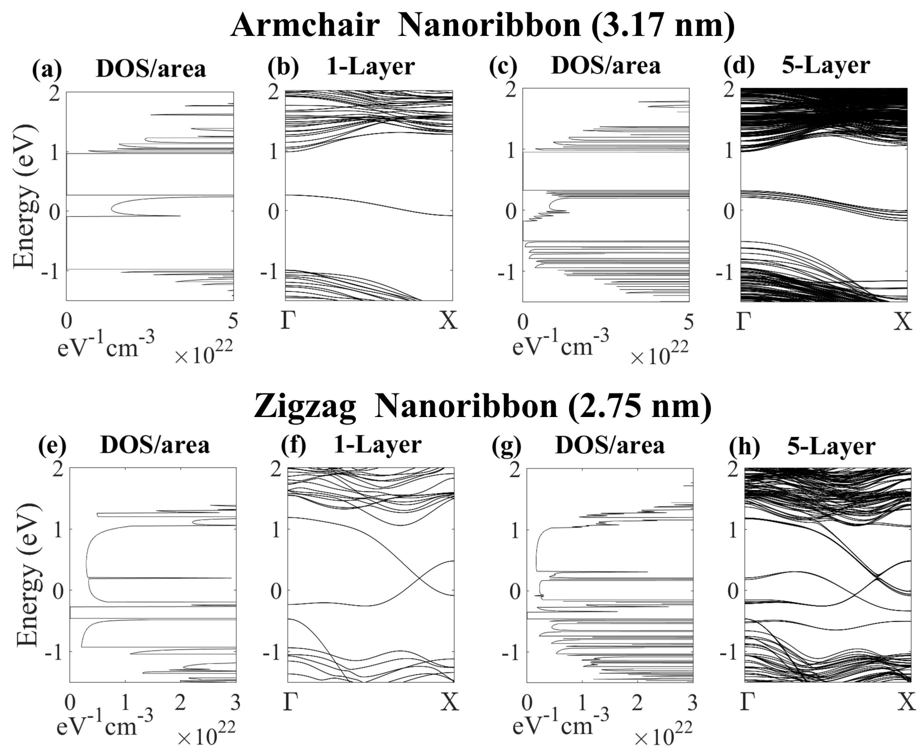

Figure 4.18: Density-of-state per area of (a) 1-layer, (c) 5-layer armchair nanoribbon, and the band diagram of (b) 1-layer, (d) 5-layer armchair nanoribbon (width = 3.17 nm). Density-of-state per area of (e) 1-layer, (g) 5-layer zigzag nanoribbon, and the band diagram of (f) 1-layer, (h) 5-layer zigzag nanoribbon (width = 2.75 nm).

doi:10.6342/NTU201700233

Chapter 5 Conclusion

We established a band structure calculation tool based on the tight binding method. Given the bulk material parameters fitted by first-principle results or experiments, the model could be extended to study the quantum structure, strain effects, or surface properties. In this thesis, we first applied the first-nearest neighbor $sp^3d^5s^*$ tight binding model on silicon nanowires. It predicts that the bandgap increases due to the quantum confinement effect. The trend is the same as the one calculated by the semi-classical method which directly solves the 2D Schrödinger equation across the nanowire, where the energy splitting is inversely proportional to the wire width square. The difference is that our tight binding model can give a more correct bandgap prediction by calculating the correct effective mass with the E-k diagram. The gate voltage effect was also investigated by adding an external potential. The external potential changes the carrier distribution, reduces the bandgap, and alters the band splitting. This silicon tight binding model can be applied to the quantum transport model by combining with Non Equilibrium Green's Functions for the further researches.

Next, we applied the tight binding method to the novel 2D material

doi:10.6342/NTU201700233

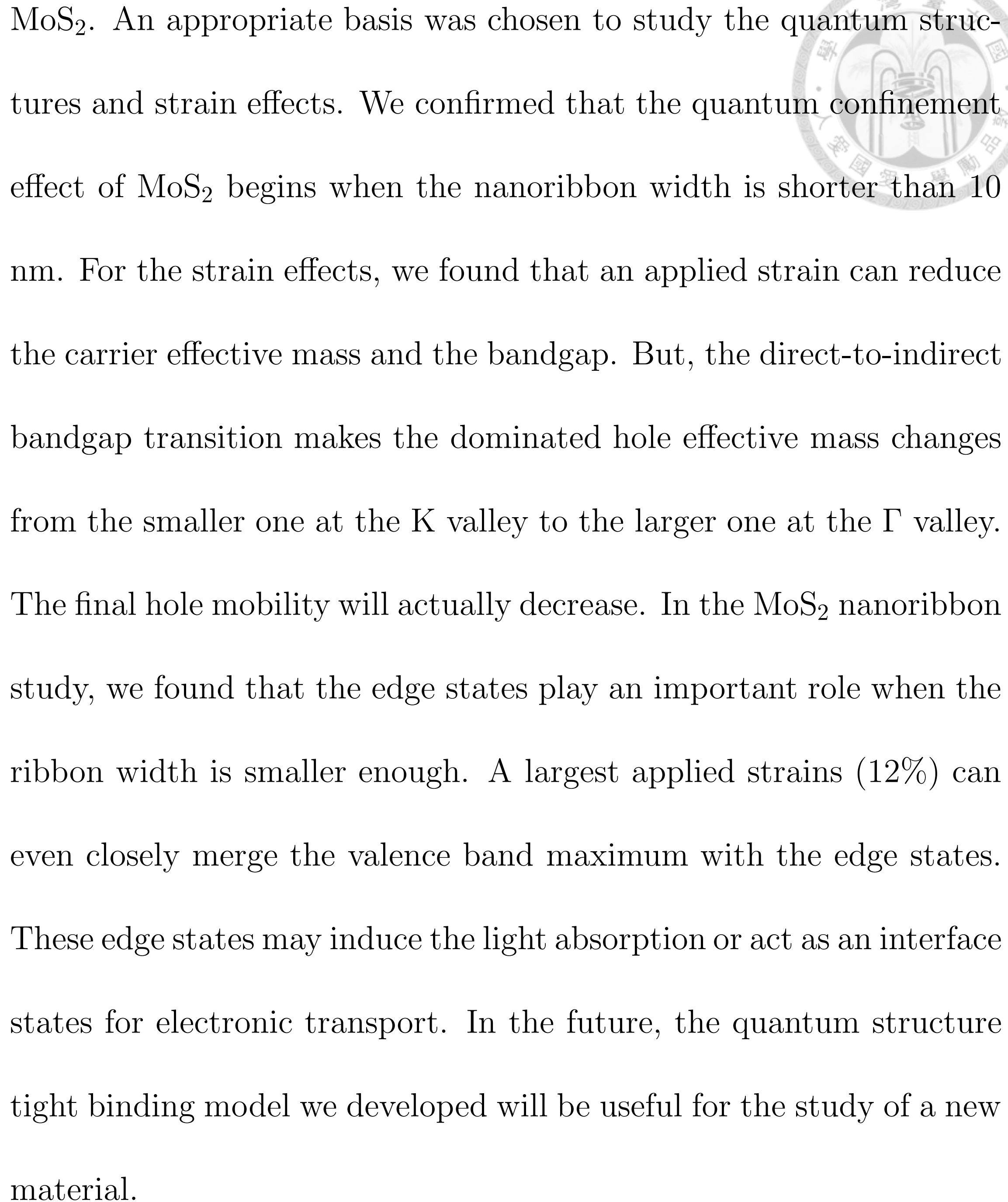

MoS_2. An appropriate basis was chosen to study the quantum structures and strain effects. We confirmed that the quantum confinement effect of MoS_2 begins when the nanoribbon width is shorter than 10 nm. For the strain effects, we found that an applied strain can reduce the carrier effective mass and the bandgap. But, the direct-to-indirect bandgap transition makes the dominated hole effective mass changes from the smaller one at the K valley to the larger one at the Γ valley. The final hole mobility will actually decrease. In the MoS_2 nanoribbon study, we found that the edge states play an important role when the ribbon width is smaller enough. A largest applied strains (12%) can even closely merge the valence band maximum with the edge states. These edge states may induce the light absorption or act as an interface states for electronic transport. In the future, the quantum structure tight binding model we developed will be useful for the study of a new material.

doi:10.6342/NTU201700233

A.1 Appendices

A.1.1 Tight Binding Parameters

Silicon	
Es	-2.15168
Ep	4.22925
Es*	19.1165
Ed	13.7895
ssσ	-1.95933
s*s*σ	-4.24135
ss*σ	-1.5223
spσ	3.02562
s*pσ	3.15565
sdσ	-2.28485
s*dσ	-0.80993
ppσ	4.10364
ppπ	-1.51801
dpσ	-1.35554
pdπ	2.38479
ddσ	-1.68136
ddπ	2.5888
ddδ	-1.814
λ	0.01989

doi:10.6342/NTU201700233

MoS_2				
	E_s	E_p	E_d	λ_{so}
Mo	5.5994	6.7128	2.6429	1.0675
S	7.6595	-2.1537	8.7689	0.2129
	E_1(Mo,Mo)	E_1(Mo,S)	E_1(S,S)	E_2(S,S)
ssσ	0.1768	-0.0917	0.3093	0.3207
spσ	1.091	1.6515	-0.921	-0.1302
psσ	-1.091	-0.6656	0.921	0.1302
ppσ	-0.3842	1.4008	0.7132	0.7053
ppπ	0.5203	-0.4812	-0.192	-0.098
sdσ	-0.5635	-1.0654	-0.2016	0.1164
dsσ	-0.5635	0.2177	-0.2016	0.1164
pdσ	-0.2316	-2.1898	-0.5204	-0.0334
dpσ	0.2316	2.8732	0.5204	0.0334
pdπ	0.0582	1.9408	-0.1203	-0.037
dpπ	-0.0582	-0.7739	0.1203	0.037
ddσ	0.3602	-3.1425	0.8347	-0.23
ddπ	0.0432	2.4975	0.7434	0.005
ddδ	0.1008	-0.3703	-0.1919	-0.1104

doi:10.6342/NTU201700233

MoS_2				
	O_1(Mo-Mo)	O_1(Mo-S)	O_1(S-S)	O_2(S,S)
ssσ	-0.0575	0.0294	-0.0532	-0.143
spσ	0.0057	-0.1765	0.024	0.0196
psσ	-0.0057	-0.1042	-0.024	-0.0196
ppσ	0.0296	-0.1865	0.0478	-0.0486
ppπ	0.0946	0.0303	-0.0104	0.0117
sdσ	-0.1082	-0.1432	0.0946	0.0297
dsσ	-0.1082	-0.048	0.0946	0.0297
pdσ	0.0212	-0.2002	0.0724	-0.0087
dpσ	-0.0212	-0.0942	-0.0724	0.0087
pdπ	-0.0448	0.2435	0.0772	-0.0031
dpπ	0.0448	-0.0132	-0.0772	0.0031
ddσ	-0.0216	0.0273	0.1849	0.006
ddπ	-0.0285	0.194	-0.0429	-0.0378
ddδ	0.0432	0.1261	-0.0333	0.0007

doi:10.6342/NTU201700233

Bibliography

[1] F. Schwierz, "Nanoelectronics: flat transistors get off the ground," *Nature nanotechnology*, vol. 6, no. 3, pp. 135–136, 2011.

[2] P. Vogl, H. P. Hjalmarson, and J. D. Dow, "A semi-empirical tight-binding theory of the electronic structure of semiconductors," *Journal of Physics and Chemistry of Solids*, vol. 44, no. 5, pp. 365–378, 1983.

[3] S. Y. Ren, X. Chen, and J. D. Dow, "Tight-binding sp^3d^5 Hamiltonian for Si," *Journal of Physics and Chemistry of Solids*, vol. 59, no. 3, pp. 403–410, 1998.

[4] J.-M. Jancu, R. Scholz, F. Beltram, and F. Bassani, "Empirical spds* tight-binding calculation for cubic semiconductors: General method and material parameters," *Physical Review B*, vol. 57, no. 11, p. 6493, 1998.

[5] R. Roldán, A. Castellanos-Gomez, E. Cappelluti, and F. Guinea, "Strain engineering in semiconducting two-dimensional crystals," *Journal of Physics: Condensed Matter*, vol. 27, no. 31, p. 313201, 2015.

doi:10.6342/NTU201700233

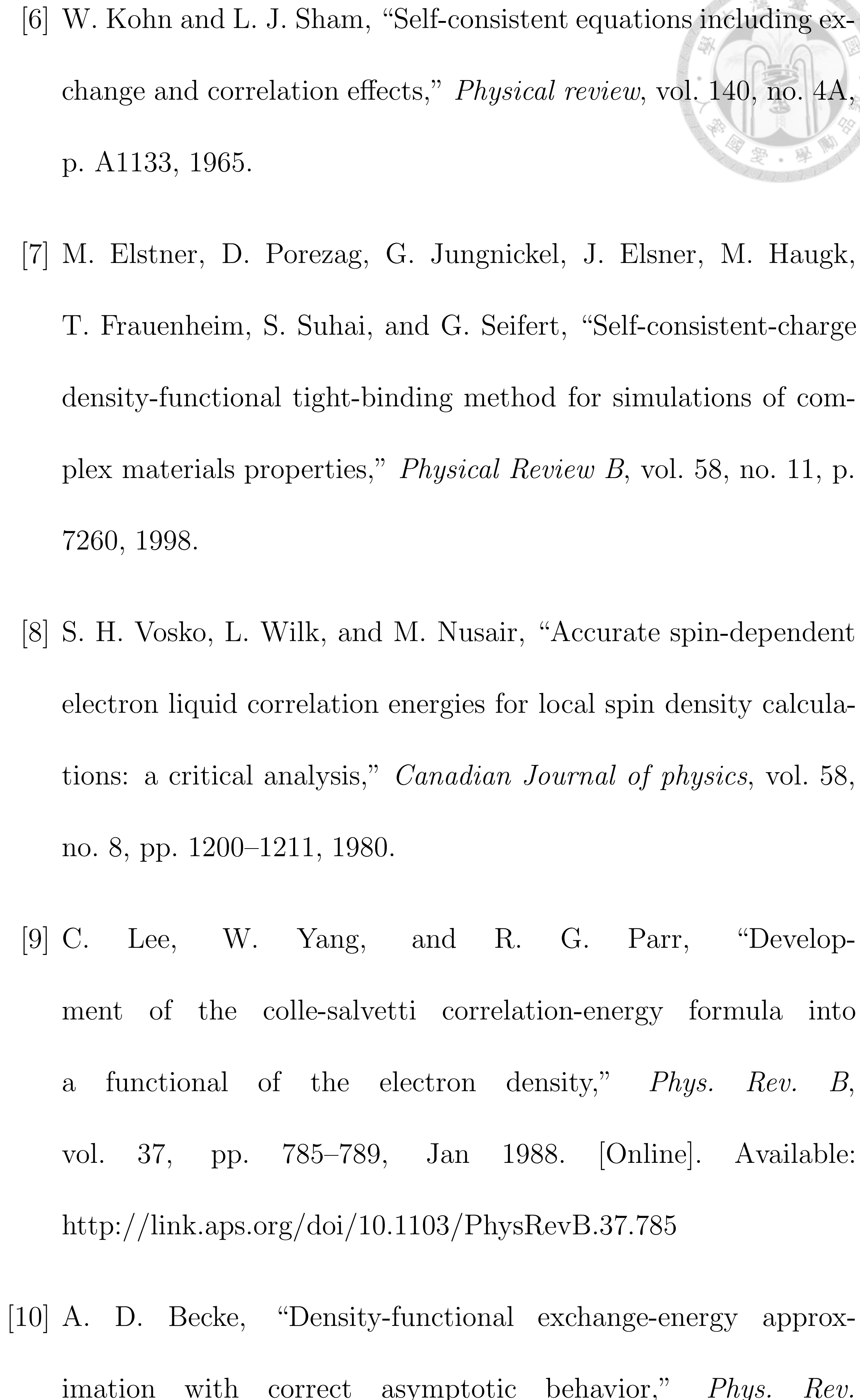

[6] W. Kohn and L. J. Sham, "Self-consistent equations including exchange and correlation effects," *Physical review*, vol. 140, no. 4A, p. A1133, 1965.

[7] M. Elstner, D. Porezag, G. Jungnickel, J. Elsner, M. Haugk, T. Frauenheim, S. Suhai, and G. Seifert, "Self-consistent-charge density-functional tight-binding method for simulations of complex materials properties," *Physical Review B*, vol. 58, no. 11, p. 7260, 1998.

[8] S. H. Vosko, L. Wilk, and M. Nusair, "Accurate spin-dependent electron liquid correlation energies for local spin density calculations: a critical analysis," *Canadian Journal of physics*, vol. 58, no. 8, pp. 1200–1211, 1980.

[9] C. Lee, W. Yang, and R. G. Parr, "Development of the colle-salvetti correlation-energy formula into a functional of the electron density," *Phys. Rev. B*, vol. 37, pp. 785–789, Jan 1988. [Online]. Available: http://link.aps.org/doi/10.1103/PhysRevB.37.785

[10] A. D. Becke, "Density-functional exchange-energy approximation with correct asymptotic behavior," *Phys. Rev.*

doi:10.6342/NTU201700233

A, vol. 38, pp. 3098–3100, Sep 1988. [Online]. Available: http://link.aps.org/doi/10.1103/PhysRevA.38.3098

[11] J. P. Perdew and W. Yue, "Accurate and simple density functional for the electronic exchange energy: Generalized gradient approximation," *Phys. Rev. B*, vol. 33, pp. 8800–8802, Jun 1986. [Online]. Available: http://link.aps.org/doi/10.1103/PhysRevB.33.8800

[12] J. P. Perdew and A. Zunger, "Self-interaction correction to density-functional approximations for many-electron systems," *Phys. Rev. B*, vol. 23, pp. 5048–5079, May 1981. [Online]. Available: http://link.aps.org/doi/10.1103/PhysRevB.23.5048

[13] F. Bloch, "Über die quantenmechanik der elektronen in kristallgittern," *Zeitschrift für physik*, vol. 52, no. 7-8, pp. 555–600, 1929.

[14] H. Hellmann, "A new approximation method in the problem of many electrons," *The Journal of Chemical Physics*, vol. 3, no. 1, pp. 61–61, 1935.

[15] J. C. Slater and G. F. Koster, "Simplified LCAO method for the periodic potential problem," *Physical Review*, vol. 94, no. 6, p. 1498, 1954.

doi:10.6342/NTU201700233

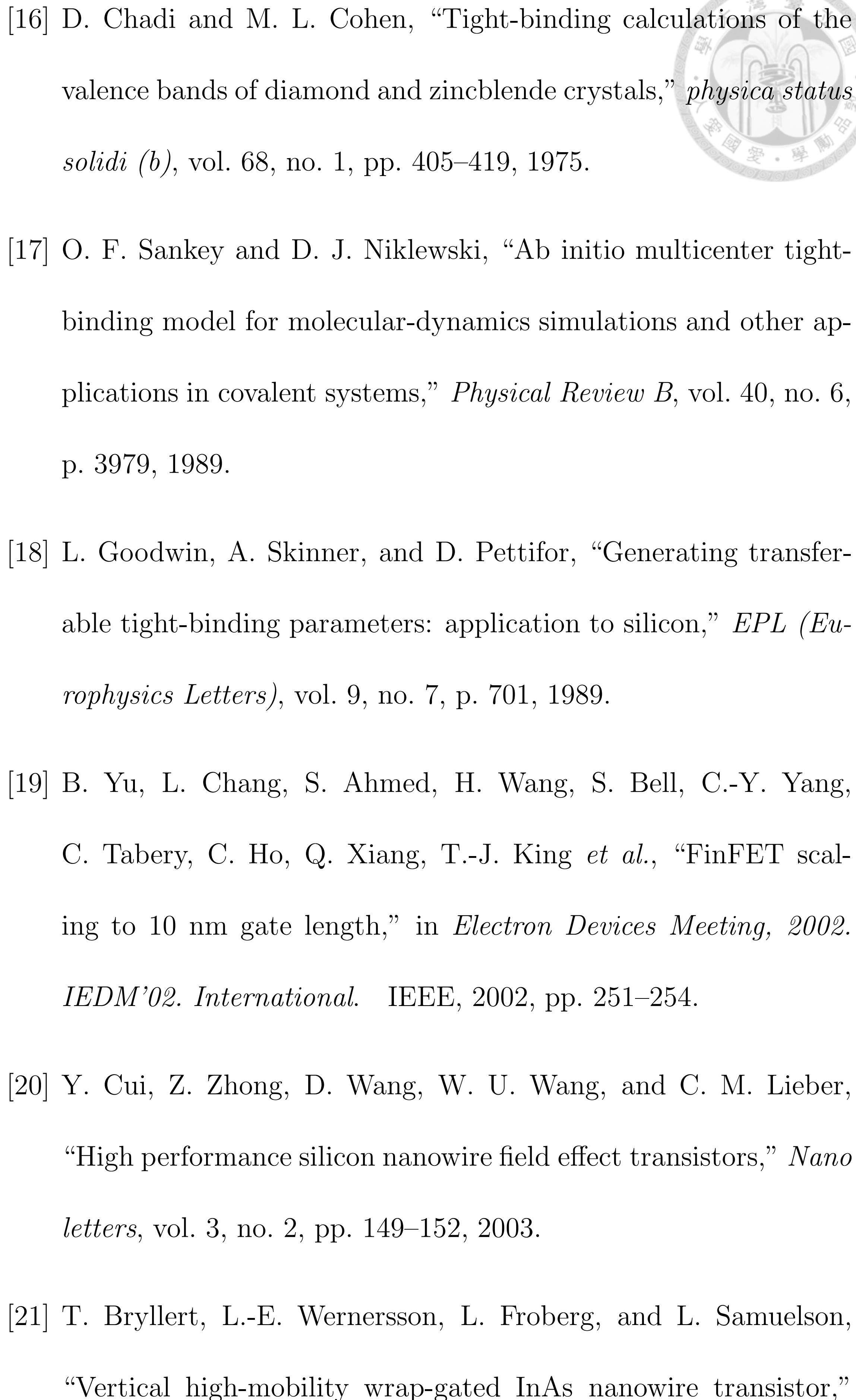

[16] D. Chadi and M. L. Cohen, "Tight-binding calculations of the valence bands of diamond and zincblende crystals," *physica status solidi (b)*, vol. 68, no. 1, pp. 405–419, 1975.

[17] O. F. Sankey and D. J. Niklewski, "Ab initio multicenter tight-binding model for molecular-dynamics simulations and other applications in covalent systems," *Physical Review B*, vol. 40, no. 6, p. 3979, 1989.

[18] L. Goodwin, A. Skinner, and D. Pettifor, "Generating transferable tight-binding parameters: application to silicon," *EPL (Europhysics Letters)*, vol. 9, no. 7, p. 701, 1989.

[19] B. Yu, L. Chang, S. Ahmed, H. Wang, S. Bell, C.-Y. Yang, C. Tabery, C. Ho, Q. Xiang, T.-J. King *et al.*, "FinFET scaling to 10 nm gate length," in *Electron Devices Meeting, 2002. IEDM'02. International.* IEEE, 2002, pp. 251–254.

[20] Y. Cui, Z. Zhong, D. Wang, W. U. Wang, and C. M. Lieber, "High performance silicon nanowire field effect transistors," *Nano letters*, vol. 3, no. 2, pp. 149–152, 2003.

[21] T. Bryllert, L.-E. Wernersson, L. Froberg, and L. Samuelson, "Vertical high-mobility wrap-gated InAs nanowire transistor,"

doi:10.6342/NTU201700233

IEEE Electron Device Letters, vol. 27, no. 5, pp. 323–325, 2006.

[22] J. Xiang, W. Lu, Y. Hu, Y. Wu, H. Yan, and C. M. Lieber, "Ge/Si nanowire heterostructures as high-performance field-effect transistors," *Nature*, vol. 441, no. 7092, pp. 489–493, 2006.

[23] F. Capasso and R. A. Kiehl, "Resonant tunneling transistor with quantum well base and high-energy injection: A new negative differential resistance device," *Journal of Applied Physics*, vol. 58, no. 3, pp. 1366–1368, 1985.

[24] B. Radisavljevic, A. Radenovic, J. Brivio, i. V. Giacometti, and A. Kis, "Single-layer MoS_2 transistors," *Nature nanotechnology*, vol. 6, no. 3, pp. 147–150, 2011.

[25] N. F. Yuan, K. F. Mak, and K. T. Law, "Possible topological superconducting phases of MoS_2," *Physical review letters*, vol. 113, no. 9, p. 097001, 2014.

[26] M. Bollinger, J. Lauritsen, K. W. Jacobsen, J. K. Nørskov, S. Helveg, and F. Besenbacher, "One-dimensional metallic edge states in MoS_2," *Physical review letters*, vol. 87, no. 19, p. 196803, 2001.

doi:10.6342/NTU201700233

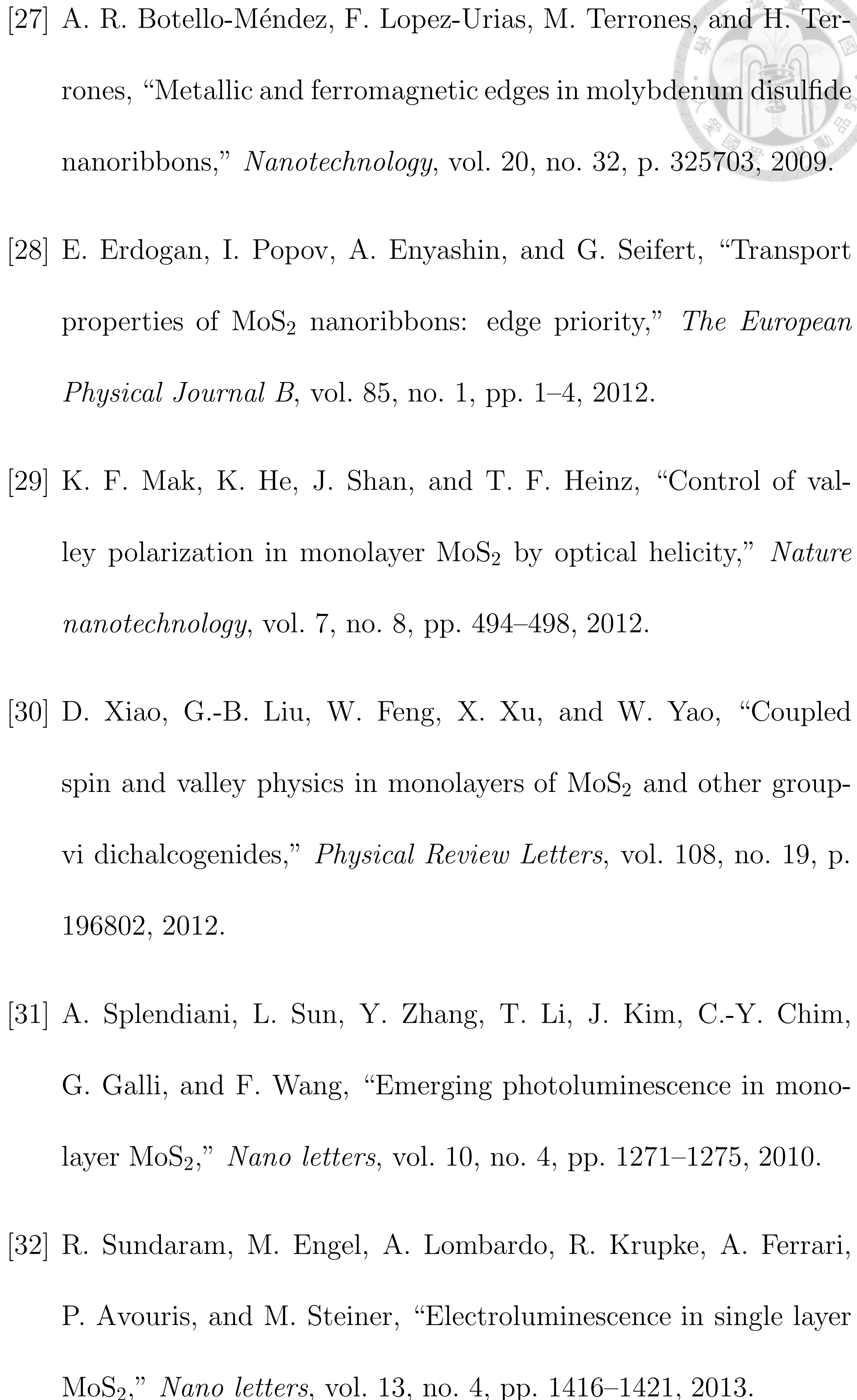

[27] A. R. Botello-Méndez, F. Lopez-Urias, M. Terrones, and H. Terrones, "Metallic and ferromagnetic edges in molybdenum disulfide nanoribbons," *Nanotechnology*, vol. 20, no. 32, p. 325703, 2009.

[28] E. Erdogan, I. Popov, A. Enyashin, and G. Seifert, "Transport properties of MoS_2 nanoribbons: edge priority," *The European Physical Journal B*, vol. 85, no. 1, pp. 1–4, 2012.

[29] K. F. Mak, K. He, J. Shan, and T. F. Heinz, "Control of valley polarization in monolayer MoS_2 by optical helicity," *Nature nanotechnology*, vol. 7, no. 8, pp. 494–498, 2012.

[30] D. Xiao, G.-B. Liu, W. Feng, X. Xu, and W. Yao, "Coupled spin and valley physics in monolayers of MoS_2 and other group-vi dichalcogenides," *Physical Review Letters*, vol. 108, no. 19, p. 196802, 2012.

[31] A. Splendiani, L. Sun, Y. Zhang, T. Li, J. Kim, C.-Y. Chim, G. Galli, and F. Wang, "Emerging photoluminescence in monolayer MoS_2," *Nano letters*, vol. 10, no. 4, pp. 1271–1275, 2010.

[32] R. Sundaram, M. Engel, A. Lombardo, R. Krupke, A. Ferrari, P. Avouris, and M. Steiner, "Electroluminescence in single layer MoS_2," *Nano letters*, vol. 13, no. 4, pp. 1416–1421, 2013.

doi:10.6342/NTU201700233

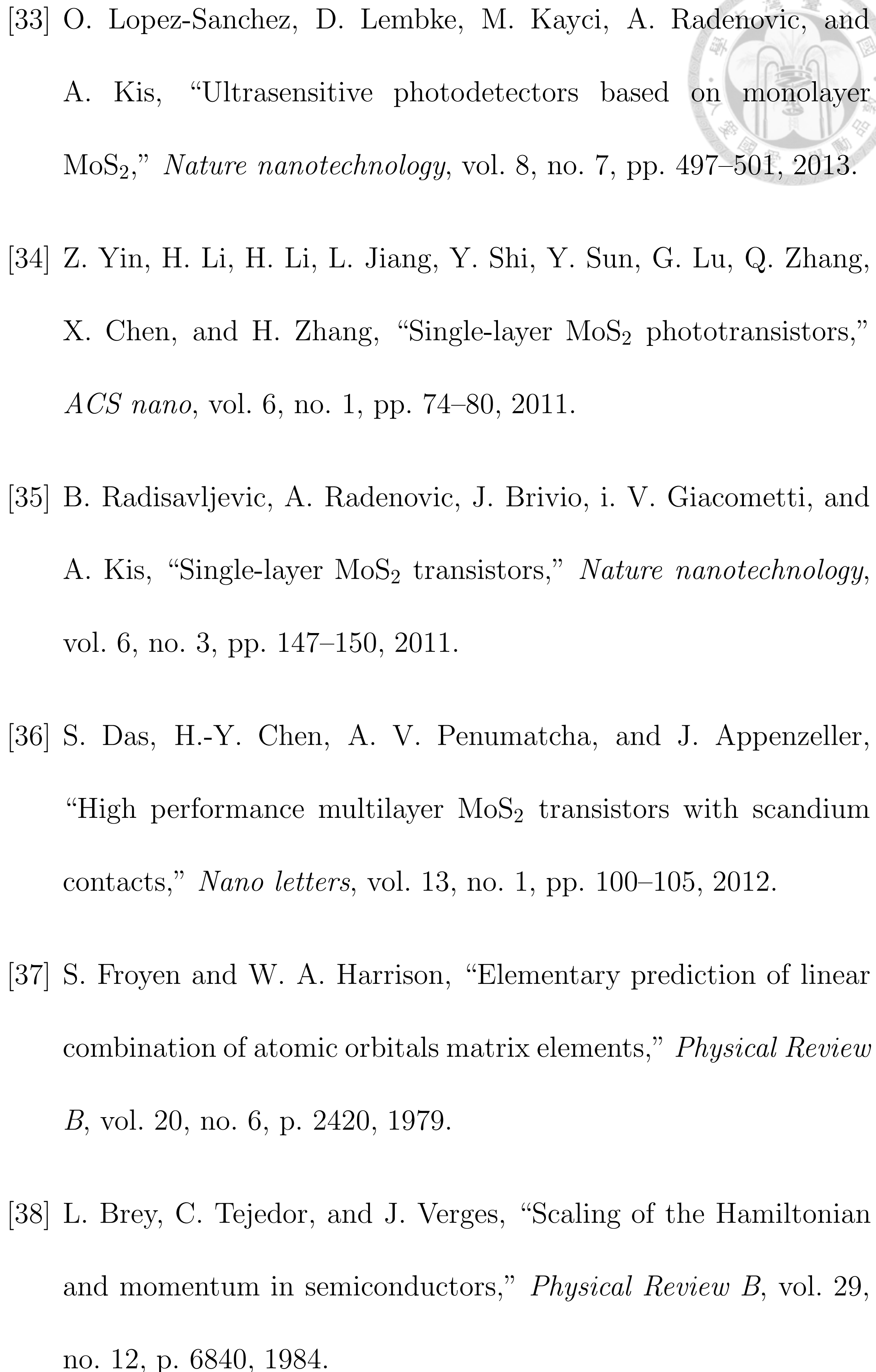

[33] O. Lopez-Sanchez, D. Lembke, M. Kayci, A. Radenovic, and A. Kis, "Ultrasensitive photodetectors based on monolayer MoS_2," *Nature nanotechnology*, vol. 8, no. 7, pp. 497–501, 2013.

[34] Z. Yin, H. Li, H. Li, L. Jiang, Y. Shi, Y. Sun, G. Lu, Q. Zhang, X. Chen, and H. Zhang, "Single-layer MoS_2 phototransistors," *ACS nano*, vol. 6, no. 1, pp. 74–80, 2011.

[35] B. Radisavljevic, A. Radenovic, J. Brivio, i. V. Giacometti, and A. Kis, "Single-layer MoS_2 transistors," *Nature nanotechnology*, vol. 6, no. 3, pp. 147–150, 2011.

[36] S. Das, H.-Y. Chen, A. V. Penumatcha, and J. Appenzeller, "High performance multilayer MoS_2 transistors with scandium contacts," *Nano letters*, vol. 13, no. 1, pp. 100–105, 2012.

[37] S. Froyen and W. A. Harrison, "Elementary prediction of linear combination of atomic orbitals matrix elements," *Physical Review B*, vol. 20, no. 6, p. 2420, 1979.

[38] L. Brey, C. Tejedor, and J. Verges, "Scaling of the Hamiltonian and momentum in semiconductors," *Physical Review B*, vol. 29, no. 12, p. 6840, 1984.

doi:10.6342/NTU201700233

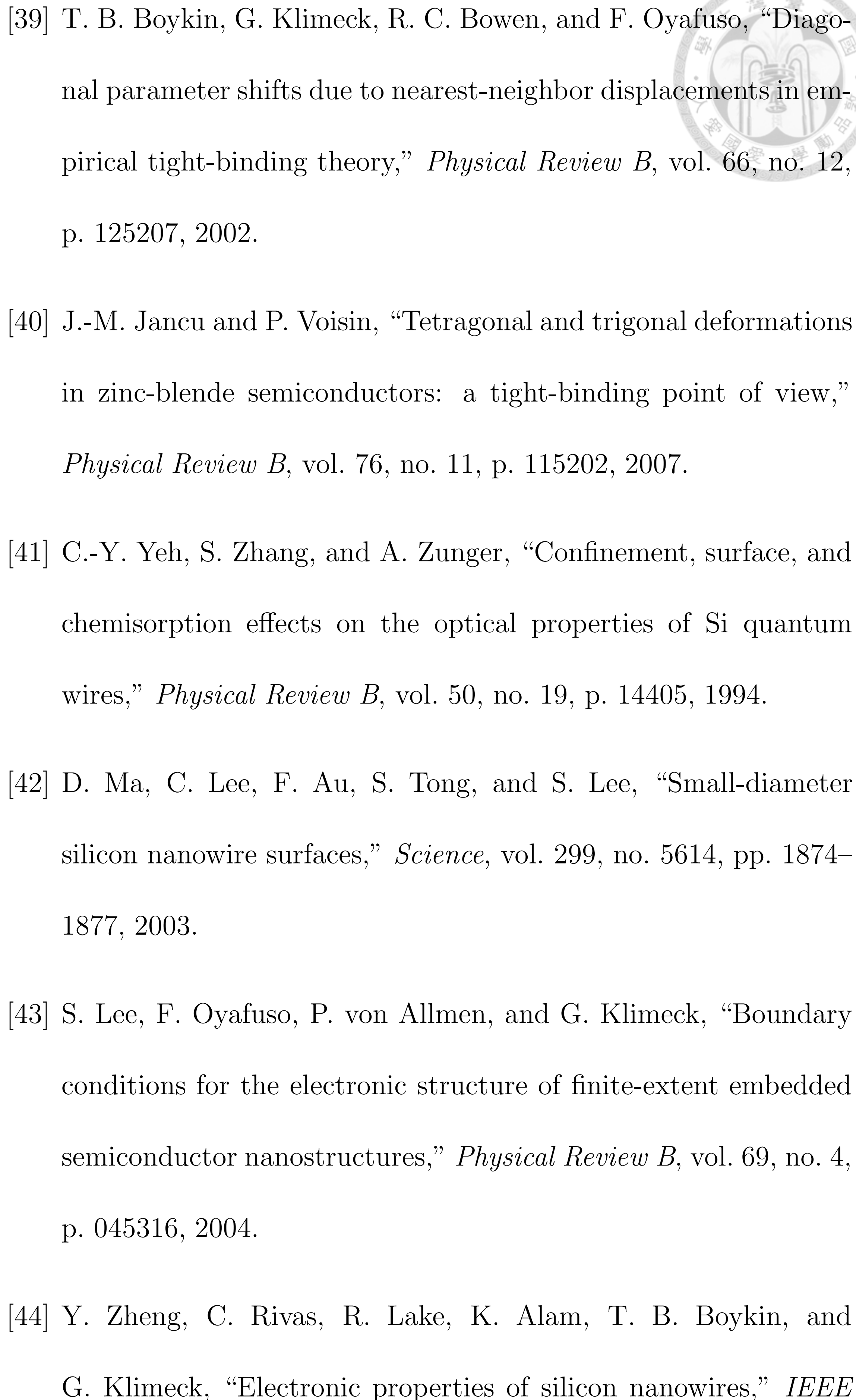

[39] T. B. Boykin, G. Klimeck, R. C. Bowen, and F. Oyafuso, "Diagonal parameter shifts due to nearest-neighbor displacements in empirical tight-binding theory," *Physical Review B*, vol. 66, no. 12, p. 125207, 2002.

[40] J.-M. Jancu and P. Voisin, "Tetragonal and trigonal deformations in zinc-blende semiconductors: a tight-binding point of view," *Physical Review B*, vol. 76, no. 11, p. 115202, 2007.

[41] C.-Y. Yeh, S. Zhang, and A. Zunger, "Confinement, surface, and chemisorption effects on the optical properties of Si quantum wires," *Physical Review B*, vol. 50, no. 19, p. 14405, 1994.

[42] D. Ma, C. Lee, F. Au, S. Tong, and S. Lee, "Small-diameter silicon nanowire surfaces," *Science*, vol. 299, no. 5614, pp. 1874–1877, 2003.

[43] S. Lee, F. Oyafuso, P. von Allmen, and G. Klimeck, "Boundary conditions for the electronic structure of finite-extent embedded semiconductor nanostructures," *Physical Review B*, vol. 69, no. 4, p. 045316, 2004.

[44] Y. Zheng, C. Rivas, R. Lake, K. Alam, T. B. Boykin, and G. Klimeck, "Electronic properties of silicon nanowires," *IEEE*

doi:10.6342/NTU201700233

transactions on electron devices, vol. 52, no. 6, pp. 1097–1103, 2005.

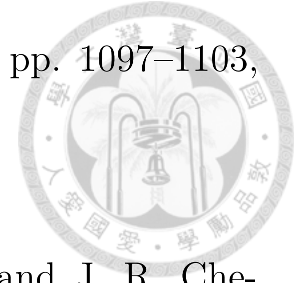

[45] S. L. Richardson, M. L. Cohen, S. G. Louie, and J. R. Chelikowsky, "Electron charge densities at conduction-band edges of semiconductors," *Physical Review B*, vol. 33, no. 2, p. 1177, 1986.

[46] T. B. Boykin and G. Klimeck, "Practical application of zone-folding concepts in tight-binding calculations," *Physical Review B*, vol. 71, no. 11, p. 115215, 2005.

[47] A. Ajoy, K. V. Murali, and S. Karmalkar, "Brillouin zone unfolding of complex bands in a nearest neighbour tight binding scheme," *Journal of Physics: Condensed Matter*, vol. 24, no. 5, p. 055504, 2012.

[48] C.-C. Lee, Y. Yamada-Takamura, and T. Ozaki, "Unfolding method for first-principles LCAO electronic structure calculations," *Journal of Physics: Condensed Matter*, vol. 25, no. 34, p. 345501, 2013.

[49] T. B. Boykin, G. Klimeck, M. Eriksson, M. Friesen, S. Coppersmith, P. von Allmen, F. Oyafuso, and S. Lee, "Valley splitting in

doi:10.6342/NTU201700233

strained silicon quantum wells," *Applied Physics Letters*, vol. 84, no. 1, pp. 115–117, 2004.

[50] N. Neophytou, A. Paul, M. S. Lundstrom, and G. Klimeck, "Bandstructure effects in silicon nanowire electron transport," *IEEE Transactions on electron devices*, vol. 55, no. 6, pp. 1286–1297, 2008.

[51] F. Zahid, L. Liu, Y. Zhu, J. Wang, and H. Guo, "A generic tight-binding model for monolayer, bilayer and bulk MoS_2," *AIP Advances*, vol. 3, no. 5, p. 052111, 2013.

[52] Z. Zhu, Y. Cheng, and U. Schwingenschlögl, "Giant spin-orbit-induced spin splitting in two-dimensional transition-metal dichalcogenide semiconductors," *Physical Review B*, vol. 84, no. 15, p. 153402, 2011.

[53] G.-B. Liu, W.-Y. Shan, Y. Yao, W. Yao, and D. Xiao, "Three-band tight-binding model for monolayers of group-VIB transition metal dichalcogenides," *Physical Review B*, vol. 88, no. 8, p. 085433, 2013.

[54] E. Ridolfi, D. Le, T. Rahman, E. Mucciolo, and C. Lewenkopf, "A tight-binding model for MoS_2 monolayers," *Journal of Physics:*

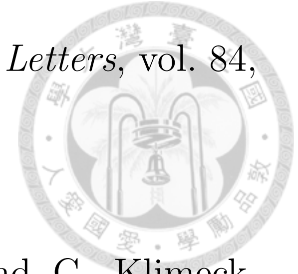

doi:10.6342/NTU201700233

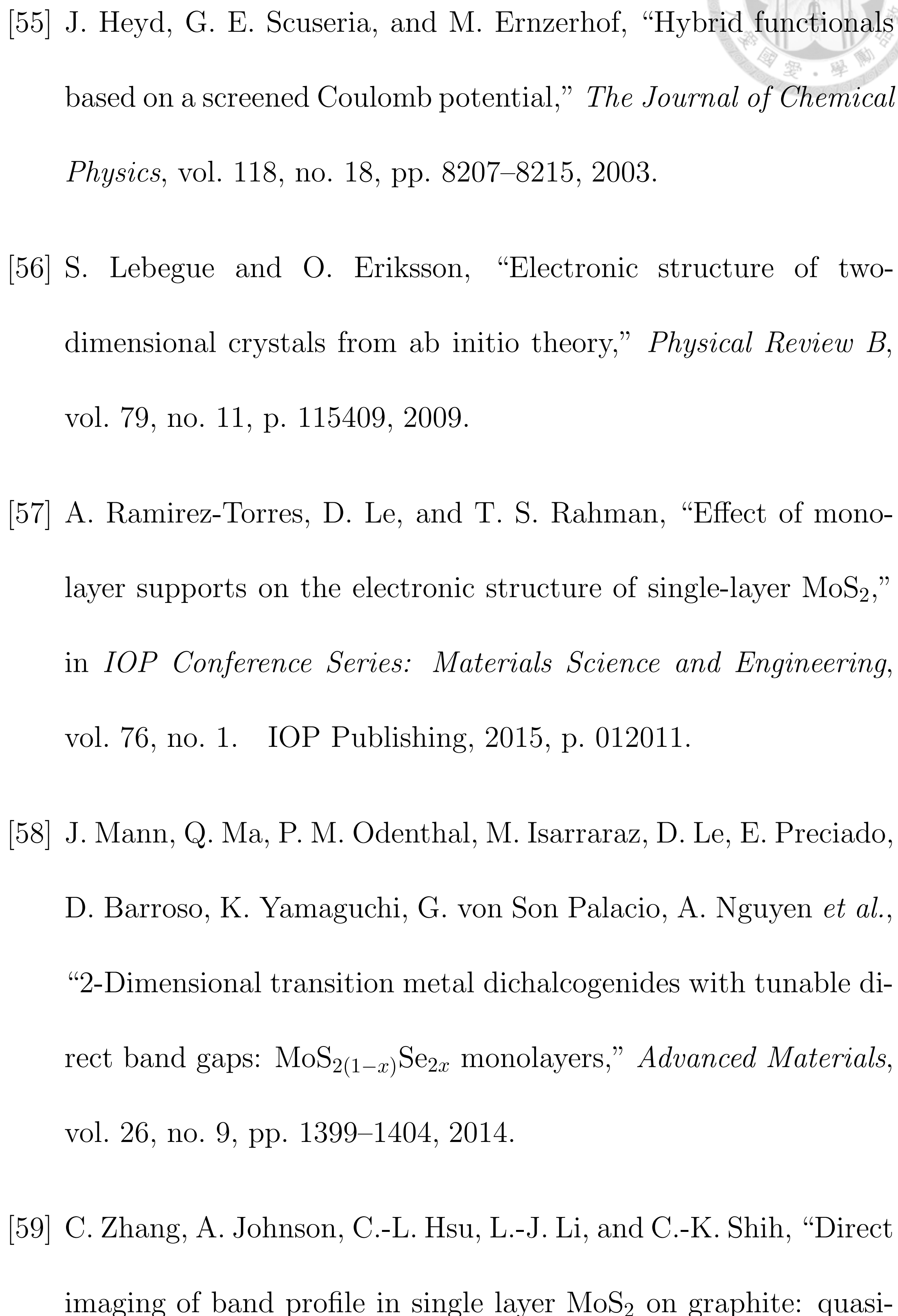

Condensed Matter, vol. 27, no. 36, p. 365501, 2015.

[55] J. Heyd, G. E. Scuseria, and M. Ernzerhof, "Hybrid functionals based on a screened Coulomb potential," *The Journal of Chemical Physics*, vol. 118, no. 18, pp. 8207–8215, 2003.

[56] S. Lebegue and O. Eriksson, "Electronic structure of two-dimensional crystals from ab initio theory," *Physical Review B*, vol. 79, no. 11, p. 115409, 2009.

[57] A. Ramirez-Torres, D. Le, and T. S. Rahman, "Effect of monolayer supports on the electronic structure of single-layer MoS_2," in *IOP Conference Series: Materials Science and Engineering*, vol. 76, no. 1. IOP Publishing, 2015, p. 012011.

[58] J. Mann, Q. Ma, P. M. Odenthal, M. Isarraraz, D. Le, E. Preciado, D. Barroso, K. Yamaguchi, G. von Son Palacio, A. Nguyen *et al.*, "2-Dimensional transition metal dichalcogenides with tunable direct band gaps: $MoS_{2(1-x)}Se_{2x}$ monolayers," *Advanced Materials*, vol. 26, no. 9, pp. 1399–1404, 2014.

[59] C. Zhang, A. Johnson, C.-L. Hsu, L.-J. Li, and C.-K. Shih, "Direct imaging of band profile in single layer MoS_2 on graphite: quasi-

doi:10.6342/NTU201700233

particle energy gap, metallic edge states, and edge band bending," *Nano letters*, vol. 14, no. 5, pp. 2443–2447, 2014.

[60] H.-P. Komsa and A. V. Krasheninnikov, "Effects of confinement and environment on the electronic structure and exciton binding energy of MoS_2 from first principles," *Physical Review B*, vol. 86, no. 24, p. 241201, 2012.

[61] A. Ramasubramaniam, "Large excitonic effects in monolayers of molybdenum and tungsten dichalcogenides," *Physical Review B*, vol. 86, no. 11, p. 115409, 2012.

[62] M. M. Ugeda, A. J. Bradley, S.-F. Shi, H. Felipe, Y. Zhang, D. Y. Qiu, W. Ruan, S.-K. Mo, Z. Hussain, Z.-X. Shen *et al.*, "Giant bandgap renormalization and excitonic effects in a monolayer transition metal dichalcogenide semiconductor," *Nature materials*, vol. 13, no. 12, pp. 1091–1095, 2014.

[63] T. Li, "Ideal strength and phonon instability in single-layer MoS_2," *Physical Review B*, vol. 85, no. 23, p. 235407, 2012.

[64] S. Bertolazzi, J. Brivio, and A. Kis, "Stretching and breaking of ultrathin MoS_2," *ACS nano*, vol. 5, no. 12, pp. 9703–9709, 2011.

doi:10.6342/NTU201700233

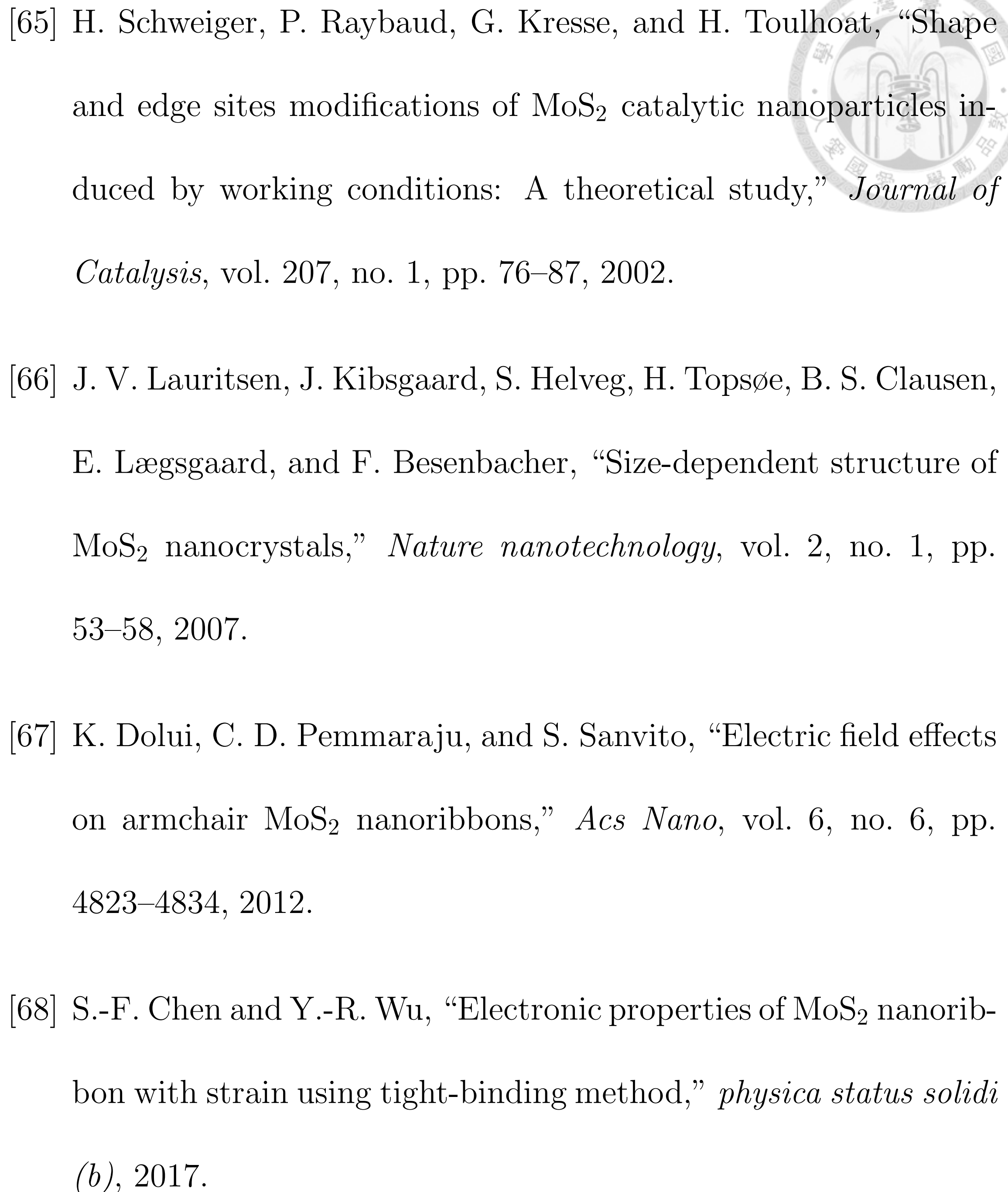

[65] H. Schweiger, P. Raybaud, G. Kresse, and H. Toulhoat, "Shape and edge sites modifications of MoS_2 catalytic nanoparticles induced by working conditions: A theoretical study," *Journal of Catalysis*, vol. 207, no. 1, pp. 76–87, 2002.

[66] J. V. Lauritsen, J. Kibsgaard, S. Helveg, H. Topsøe, B. S. Clausen, E. Lægsgaard, and F. Besenbacher, "Size-dependent structure of MoS_2 nanocrystals," *Nature nanotechnology*, vol. 2, no. 1, pp. 53–58, 2007.

[67] K. Dolui, C. D. Pemmaraju, and S. Sanvito, "Electric field effects on armchair MoS_2 nanoribbons," *Acs Nano*, vol. 6, no. 6, pp. 4823–4834, 2012.

[68] S.-F. Chen and Y.-R. Wu, "Electronic properties of MoS_2 nanoribbon with strain using tight-binding method," *physica status solidi (b)*, 2017.

doi:10.6342/NTU201700233